Resonant Adaptive Mirrors

by

Amr Kamel

A thesis
presented to the University of Waterloo
in fulfillment of the
thesis requirement for the degree of
Doctor of Philosophy
in
Mechanical & Mechatronics Engineering

Waterloo, Ontario, Canada, 2020

Examining Committee Membership

The following served on the Examining Committee for this thesis. The decision of the Examining Committee is by majority vote.

External Examiner:	Dr. Yu Sun Professor, Dept. Electrical & Computer Engineering, University of Toronto,
Supervisor(s):	Mustafa Yavuz Professor, Dept. Mechanical & Mechatronics Engineering, University of Waterloo
	Eihab M. Abdel-Rahman Professor, Dept. Systems Design Engineering, University of Waterloo
Internal Member:	Stewart McLachlin Assistant Professor, Dept. Mechanical & Mechatronics Engineering, University of Waterloo
Internal-External Members:	Kostadinka Bizheva Professor, Dept. Physics & Astronomy, University of Waterloo
	Mohamed A. Basha Professor, Dept. Electrical & Computer Engineering, University of Waterloo

Auther's Declaration

I hereby declare that I am the sole author of this thesis. This is a true copy of the thesis, including any required final revisions, as accepted by my examiners.

I understand that my thesis may be made electronically available to the public.

Abstract

Deformable mirrors (DMs) are integrated into adaptive optical (AO) systems to compensate for wavefront aberrations. These aberrations degrade the image resolution of telescopes, microscopes, ophthalmoscopes, and optical coherent tomographs. The objective of the DM in these applications is to compensate for wavefront aberrations. Continuous and segmented DMs utilize a variety of mechanisms such as electrostatic, piezoelectric, and electromagnetic actuation. Micro-electromechanical systems (MEMS) DMs have the advantages of low cost, low power consumption, and high electrode density. As the electrode count increases, the possibility of the desired modes corresponding to the Zernike modes appearing increases. However, the complexity of the static actuation also increases.

In ophthalmology, fifth order Zernike modes are used to categorize the aberrations induced by the human eye. These aberrations would degrade the image resolution of the retina during laser scanning. Therefore, a dynamically continuous DMs were developed and actuated at a natural frequency corresponding to the desired Zernike mode. The actuations would drive the mirror plate to deform into the shape of the desired mode. Multiple modes corresponding to low- and high-order Zernike modes were obtained. Resonant DMs exploit the dynamic amplification available at natural frequency's in order to reduce voltage and power requirements. This will also reduce the requirements for spatial control of individual electrodes' voltage. However, the use of circular mirror plates to create the electromechanical modes has led to the appearance of degenerate modes (pairs of almost identical modes with closely spaced frequencies). Electrostatic fields were designed to separate those modes and help break coupling between them. The fields employ selectively, actuating some of the electrodes under the DM while grounding the rest. An AC voltage was applied to selective scheme of electrodes in order to induced mode shapes that are corresponding to the Zernike modes. This design relies on a new technique which uses pulsed laser scanning instead of continuous laser scanning.

The proposed DM was designed and fabricated using a Micra-GEM fabrication process. Simulations using the finite element method (FEM) software COMSOL were used in order to determine the natural frequencies and mode shapes, and to separate degenerate modes natural frequencies by applying electrostatic fields that increase the difference between them. Characterization of the DM was conducted using laser Doppler vibrometer to identify the mode shapes and its natural frequencies experimentally. The stroke measurements of the target DM were shown as a function of frequency and amplitude. In addition, RMS error measurements were used as a comparison between DM modes and there corresponding Zernike mode.

The aim of this research was to over come the influence function due to mechanical coupling in the continuous DMs. Influence function requires different voltages that apply to electrode scheme. Therefore, static actuation of the DMs rely on a complex driving circuits. Resonant DMs eliminate the effect of the influence function by triggering the mirror via its natural frequencies. They reduce the number of fired electrode scheme by applying single voltage to the electrodes. As a result, they reduce the complexity of the driving circuits that require to control its shape. This research requires a new technique of using a pulsed laser instead of a continuous laser for the proposed DM. This may lead to manipulation of the optical laser signal using the mirror as a part of the signaling process. This should be completed by synchronizing the frequencies of both the DM and the laser to produce a high resolution image of the retina.

Acknowledgements

I would like to thank my supervisors, Prof. Eihab Abdel-Rahman and Prof. Mustafa Yavuz for their guidance and help throughout this work. I am very grateful to them for spending time discussing results and sharing ideas. Also, I would like to thank my group members; Alaaeldin Ahmed, Mohamed Arabi, Resul Saritas, Ayman Alneamy, Majed Alghamdi, Hamidreza Nafissi for their help throughout this work.

Table of Contents

List of Tables

List of Figures

Chapter 1

Introduction

1.1 Background

A wavefront is a surface which encircles the optical rays with a constant phase. Plane wavefronts and spherical wavefronts are introduced by a source situated at infinity, and by a point source emanating within an optical system respectively Fig. 1.1.

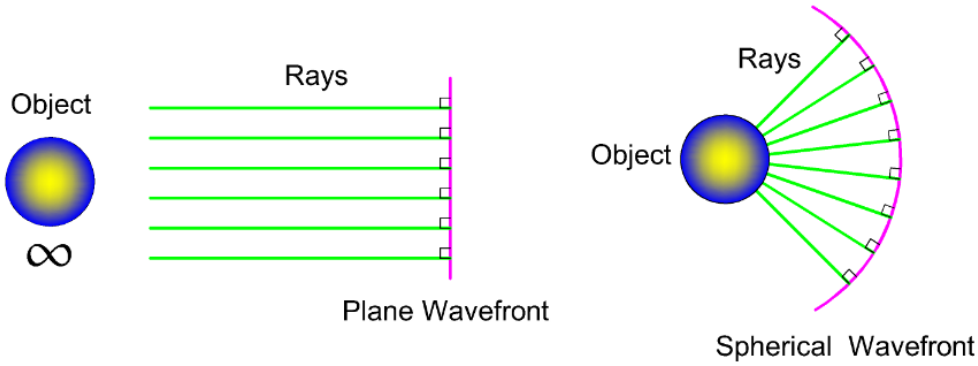

Figure 1.1: Plane wavefront and Spherical wavefront

A wavefront distortion or aberration is a change in phase of the wavefront. This change is shown as phase advance or phase lag appearing in the wavefront propagation Fig. 1.2. Aberrations are induced in the wavefront due to atmospheric turbulence, temperature variations, optical misalignments, surface polishing defects, and biological tissues. Atmospheric turbulence changes the phase of the wavefront due to the non-uniform atmosphere

of the earth [1], and the variation in temperature which causes an arbitrary fluctuation in the refractive index of the atmosphere [2]. Also, optical components such as lenses alter the wavefront phase due to differences in the optical path length at the center and tip of the edge. Biological tissues also induce aberrations in the wavefront due to inhomogeneities in the layers. For example, the cornea consists of five layers; epithelium, bowmans membrane, stroma, descemets membrane, and endothelium [3]. These layers modify the refractive index along the optical path. Furthermore, the imperfect shape of the cornea causes astigmatism [1, 3, 4].

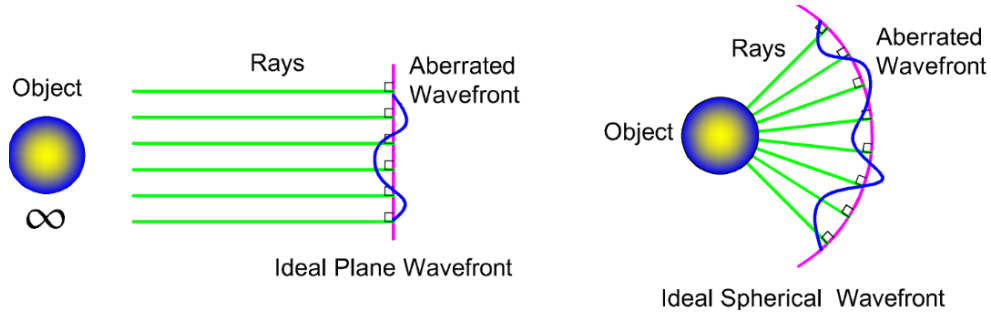

Figure 1.2: Phase change of wavefront

Aberrations can manifest as astigmatism, spherical aberration, coma, or defocus. Wavefront aberrations have a significant impact in degrading image formation. The perfect image formation is produced when the incident rays converge on a single sharp point focus at the desired image plane Fig. 1.3 (a)[1]. However, wavefront aberrations diverge the rays away from a single point due to phase changes. For instance, a spherical aberration converges a bundle of light to a point that is closer to the lens and other bundle of light converges to a point that is near to the lens. Consequently, there is no single point focus and the image appears to be blurred Fig. 1.3 (b)[2]. Another example of aberration is comatic aberration which degrades the image resolution when the light focus onto the image plane at different height Fig. 1.3 (c)[3]. Therefore, the objective of the Adaptive Optics (AO) system is to manipulate the image quality by correcting wavefront aberrations. AO are also used to overcome aberrations due to imperfections in the optical components and misalignment of optical elements. Furthermore, it compensates the wavefront aberration that are induced from biological samples and atmospheric turbulence. It can also enhance the performance of lower performance optical systems, and as a result can reduce the total cost of optical

[1] A permission is shown in Appendix A Fig. A.1
[2] A permission is shown in Appendix A Fig. A.1
[3] A permission is shown in Appendix A Fig. A.1

systems [6]. This system can be found in many applications such as astronomy, biology, and vision science. AO systems consist of three main components: a wavefront sensor to measure the wavefront aberration, a control system to track the aberration overtime, and a deformable mirror to correct the wavefront distortion as shown in Fig. 1.4[4]. A retinal image was captured without AO which shows low image resolution due to aberrations Fig. 1.5 (a)[5]. A significant improvement in image resolution is achieved by using adaptive optics scanning laser ophthalmoscope which eliminate the wavefront aberration Fig. 1.5 (b)[6].

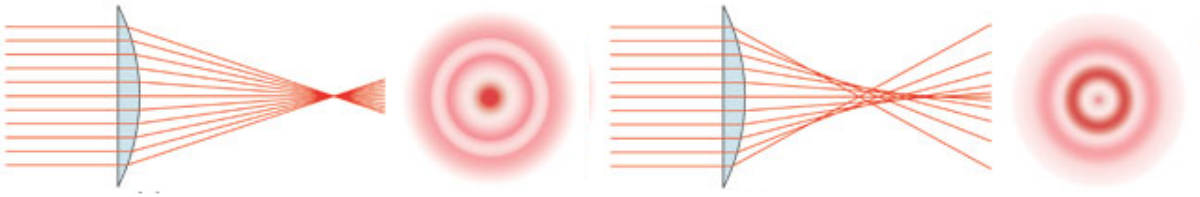

(a) Ideal wavefront without aberration

(b) Wavefront with spherical aberration

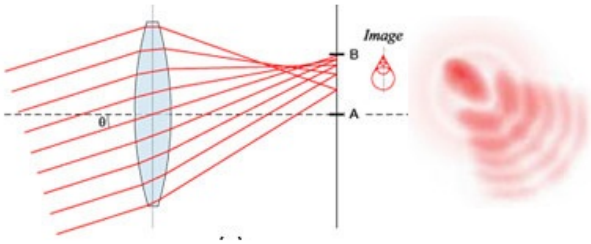

(c) Wavefront with comatic aberration

Figure 1.3: Wavefront aberrations [5]

1.2 Deformable Mirrors

In the AO system, DMs respond to specific change in its profile according to the wavefront aberration sensor signal. In order to deform the DMs, mechanisms such as piezoelectric,

[4]A permission is shown in Appendix A Fig. A.2
[5]A permission is shown in Appendix A Fig. A.2
[6]A permission is shown in Appendix A Fig. A.2

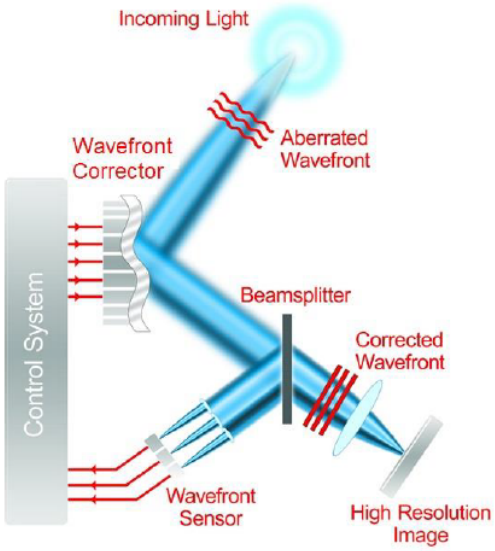

Figure 1.4: Adaptive optics (AO) system [7]

elctrostatic, and electromagnetic actuation are used. DMs are either continuous or segmented piston-tip-tilt. Mathematically, the deformed shapes of the DM are represented by Zernike polynomials which are polynomials normal to a unit circle [9]. The DM as a part of adaptive optics has been found in many apparatus such as telescopes, microscopes, adaptive optics scanning laser ophthalmoscope (AOSLO), and optical coherent tomography (OCT).

An electrostatic DM with 331 MEMS hexagonal segmented piston-tip-tilt mirror was designed for telescopic observations [10]. Each segment has a diameter of 600 μm, and excitation was applied using three rectangular electrodes underneath its geometry. This mirror has reached a perpendicular stroke of 1 μm, and a tilt inclination of ± 3 mrad with aperture of 9.5 mm. Furthermore, an electrostatic DM with 37 and 337 MEMS hexagonal segmented piston-tip-tilt mirrors were designed for use in vivo microscopes and telescopes respectively. Each segment was actuated using three rectangular electrodes, and each DM has a diameter of 750 μm, Fig. 1.6[7]. The maximum stroke is 3.5 μm, and the tilt angle is ± 8 mrad with apertures of 3.8 mm and 11.6 mm respectively. Another configuration of an electrostatic MEMS segmented DM with 140 square electrodes was incorporated in an ophthalmic equipment in order to improve the images of the retina [11]. This mirror has a maximum piston stroke of 2 μm with an operating voltage of 220 V and an aperture

[7] A permission is shown in Appendix A Fig. A.2

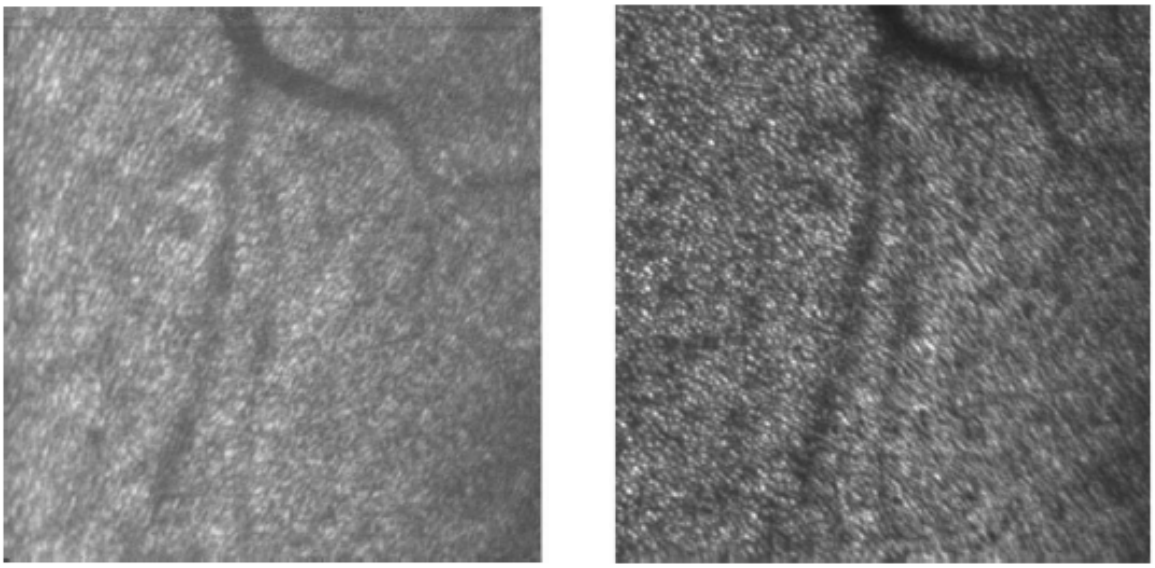

(a) Retinal image without AO

(b) Retinal image with AO

Figure 1.5: Retinal image [8]

of 3.3 mm. An electrostatic MEMS segmented piston-tip-tilt DM was used in AOSLO to correct the eye induced aberrations and enhance the retinal imaging [12]. This mirror has a 37 hexagonal mirror segments with a three diamond shaped electrodes that underlying each segment. A stroke of 5 μm, and a tilt angle of ± 5 mrad were achieved with aperture of 3.5 mm. A 91 hexagonal actuators with a thickness of 80 μm was deposited on a silicon wafer with a thickness of 700 μm and a diameter of 150 mm. The maximum operating voltage is 140 V with aperture diameter of 65 mm. An assembly can be made using a number of these segmented mirrors to build a large mirror [13].

The idea behind using different configurations of mirrors or electrodes is to increase the useful area and reduce the complexity of the control circuit. However, segmented DMs suffer from energy losses due to the fill factor between the segments. These gaps allow a bundle of rays to be diffracted. This system allows each segment to have independent motion, which is appropriate for large apertures, especially telescopes, due to ease of replacement and maintenance.

An electrostatic MEMS continuous membrane DM with 4096 square electrodes was designed for astronomy, with a maximum stroke of 4 μm, an operating voltage up to 300 V, and aperture of 19.2 mm [14]. Another version of an electrostatic MEMS contin-

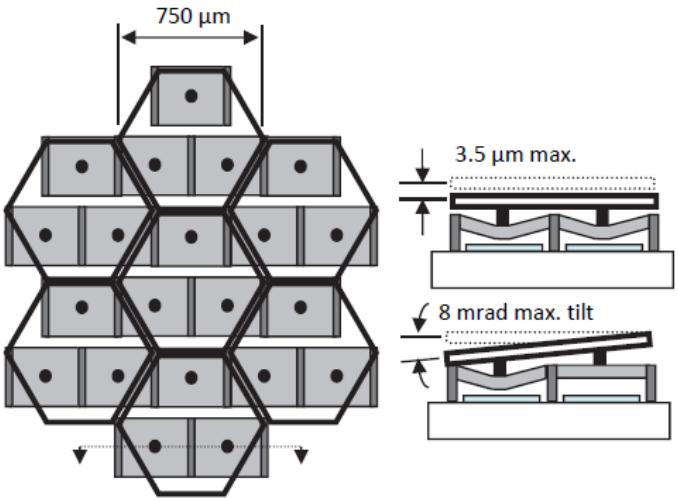

Figure 1.6: Segmented Hexagonal DM [7]

uous DM with 140 square electrodes was fabricated with a maximum piston stroke of $2\,\mu m$, a maximum voltage of 240 V, and aperture of 3.3 mm[15]. A micro-machined continuous membrane with 37 hexagonal electrodes was used to correct the ocular aberration with a stroke of $3.5\,\mu m$. This mirror was actuated using an electrostatic actuation voltage of 140 V and it has an aperture of 9.2 mm [16, 17]. A stack of lead zirconium titanate (PZT) plates were used to increase the number of actuators and stroke of the DM for astronomy application [18]. These mirrors have a range of 50 to 5000 actuators and 50 to 500 mm diameter[19]. Monomorph DM was integrated in telescopes with a single PZT plate, a 85 electrodes and a range of 25 to 250 mm diameter [18, 19]. A 19 PZT hexagonal electrode were introduced underneath a continuous DM which was used for correcting ocular aberrations. This mirror has a higher stroke of $3\,\mu m$ and $6\,\mu m$ to $8.5\,\mu m$ when the central seven electrodes and boundary electrodes were fired respectively with an operating voltage of -150 V to 450 V [17]. A stroke of $22.18\,\mu m$ for a defocus mode Z_2^0 at $\pm 125\,V$ was achieved using a 25 piezoelectric polyvinylidene fluoride (PVDF) actuation electrode with aperture of 10 mm [20]. However, an electrostriction material was used two ceramic lead magnesium niobate (PMN) layers. This mirror was used for correction of human eye aberration with a 10.2 mm pupil diameter and a $16\,\mu m$ stroke that measured when all of 35 concentric electrodes are fired [17, 21]. Two types of continuous Xinetics deformable mirrors were used in ophthalmic instrumentations and telescopes with an aperture of 75 mm and 140.208 mm, a 97 and a 349 PMN electrodes respectively, and an operating volatge of 100 V [22, 11]. A 52 electromagnetic actuators was used to excite a continuous mem-

brane deformable mirror. This mirror was utilized in ophthalmic applications with a pupil diameter of 11.89 mm and an applied voltage started from 0.25 V up to 1 V [23]. Another type of electromagnetic actuation is found using ALPAO DM97-15 continuous DM with 97 actuators and a 13.5 pupil diameter. This mirror was integrated into a combination of scanning laser ophthalmoscope (SLO) and optical coherence tomography (OCT) [24].

Continuous DMs achieve near-zero diffraction due to a fill factor of zero and sustains the continuity of the wavefront. However, it has a coupling effect as a result of exciting neighboring electrodes. Basically, the main objective of the deformable mirror is to replicate the Zernike polynomials corresponding to wavefront aberration with a large peak to valley stroke. To do so, an open loop system and closed loop system were introduced in order to control a specific Zernike mode [25, 26, 27, 28, 29, 30].

Segmented and continuous DMs are actuated using various actuation mechanisms. Electromagnetic actuation has the largest stroke which is a significant advantage. However, it requires bulky coils and permanent magnets, thereby occupying large space. Piezoelectric materials, such as PZT [13] and PVDF [20], exhibit a hysteresis requiring additional bias voltage to counter-act which complicates the process of mirror actuation and control. Electrostrictive materials, such as PMN [21], have lower hysteresis in comparison to PZT.

In general, MEMS DMs can realize lower costs and power consumption combined with higher actuator density which enables robust surface deformation. However, they are restricted by a small stroke. For ocular aberration, best performance was obtained by electromagnetic mirrors with the least residual error. The DM with 35 PMN concentric electrodes had the next favorable performance. The electrostatic DMs with 140 electrodes, electrostatic DM with 37 electrodes, and PZT DM with 37 electrodes have almost equal performances. As a result, performance of the DM depends on not only the number of electrodes and stroke but also on the actuator layout [31, 32].

Segmented and continuous DMs were fabricated using both surface micro-machining and bulk micro-machining. For instance, continuous electrostatic DMs with 140 and 4096 electrodes were fabricated using surface micro-machining with polycrystalline silicon thin films [15, 33], while bulk micro-machining fabrication process was used to produce large mirror dimensions [34, 35, 36, 37].

Most DMs used in ophthalmology are listed in Table 1.1. The objective of these mirrors is to replicate the Zernike modes in order to correct wavefront aberrations and produce high resolution images. Three major problems beset these mirrors. First, the presence and use of influence functions to represent mechanical coupling between individual electrodes and a continuous mirror surface. These functions are obtained by firing one electrode and measuring the static displacement of the mirror in response to it. The operation is

repeated for each electrode individually with different voltages. Individual Zernike modes are realized by solving a a linear system to determine the contribution of each influence function, and thus the voltage of the corresponding electrode, to the mode. Second, the requirement to supply various voltage values to different electrodes results in a highly complex electrical drive circuit. Third, determining these voltages and supplying them to the respective electrodes requires a complex control scheme.

Table 1.1: Clinical use of deformable mirror in ophthalmology

DM type	DM Φ	Stroke	Beam Φ	Actuator #	Power
Continuous (Xinetics) [38]	7.5 mm (pupil)	12-53 um / 7-11 um		14-15 / 11-14	
Segmented piston [38]	7.5 mm (pupil)	12-53 um / 7-11 um		>95 / 50-90	
Segmented piston-tip-tilt [38]	7.5 mm (pupil)	12-53 um / 7-11 um		12-19 / 9-10	
Continuous (Xinetics) [11]	75 mm	±4 um	1.9 mm	97	100 V
Segmented (BMC) [11]	3 × 3 mm	±2 um	1.9 mm	144	220 V
Continuous (BMC) [39]	4.4 mm			140	
Bimorph [40]					
MEMS (BMC) [40]					
Continuous (Xinetics) [41, 42]		2 um/actuator	1.5 mm	37 PZT	
Continuous (Xinetics) [43]		2 um/actuator	>2 mm dia	37 PMN	
Bimorph (AOptix) [44]		32 um		37	
Continuous (Xinetics) [45]				37	
AOptix [46]		16 um		37	
BMC [46]		3.8 um		140	
Bimorph (AOptix)[47, 48]	10 mm (pupil)			37	
MEMS (BMC) [47, 48]	3.1 mm pupil			144	
Segmented piston-tip-tilt (IrisAO) [49, 50, 51, 52]		5 um	2.3 mm [51]/1.2 mm [52]	111	
Continuous membrane (ALPAO) [53]	10.5 mm (pupil)	60 um	1.7 to 5 mm	69	
Membrane [54]				32	
Bimorph [54]				19 PZT	
Segmented MEMS (IrisAO) [55, 52, 56]		5 um	5.5 mm[56]/3.5 mm [52]	111	
Bimorph (AOptix) [57]	10 mm (pupil)			37	
MEMS (BMC) [57]	3.12 mm (pupil)			144	
Segmented MEMS (IrisAO) [58]			0.89 mm	111	
PMN Bimorph (AOptix) [59]	10 mm (pupil)	32 um		35	
Continuous membrane (ALPAO) [60, 24, 61, 62, 39, 63]	13.5 mm (pupil)	60 um	2 mm [61]	97	50 W
Bimorph (AOptix) [64, 65]	10 mm (pupil)				
MEMS (BMC) [64, 65]	3.125 mm (pupil)				
Continuous membrane (OKO) [16]	9.2 mm (pupil)/15 mm(total)	8 um	1.75 mm	37	250 V

1.3 Scope

DMs have to replicate the Zernike modes in order to correct for the wavefront aberrations. DMs have a stroke of at least the wavelength of the source in order to achieve a constructive interference. A statically actuated DMs are able to replicate the Zernike modes and achieve a high stroke. However, these mirrors rely on a high dense of electrodes for actuation. Furthermore, each electrode has different voltage according to its orientation to replicate a certain Zernike mode. Therefore, these mirrors require a complex algorithm due to the influence function which shows up because of mechanical coupling to control the electrode arrays in order to produce each Zernike mode individually. This control system tracks

the wavefront by deforming the DM overtime with the least amount of residual error. In order to eliminate the spatial control [66, 67] and its dependence on algorithm complexity, the use of dynamic actuation is preferable. Dynamic actuation of the DM at resonance produces a large amplitude which is greater than the wavelength of the light source. A continuous DM with 140 electrodes was tested dynamically in two photon microscopes and achieved adequate wavefront correction [68].

The proposed deformable mirror is designed to be a continuous DM which avoid signal losses in the segmented mirrors. It is applicable in ophthalmic instruments to compensate for the degradation of images due to eye induced aberrations during scanning. The proposed DM under dynamic actuation mechanism is able to replicate low order and high order Zernike modes with low number of electrodes. It shows a simple actuation mechanism by applying a single voltage to the electrodes in order to induce a certain Zernike mode individually. As a result, it reduce the complexity of algorithm to control the electrode arrays. This mirror propose a replacing of the continuous laser scan with a pulsed laser scan. The challenge is to synchronize the frequencies of the laser scanning beam and the natural frequencies of the DM in which the incident beam interfaces with the mirror surface at its maximum amplitude.

Chapter 2

Mirror Design and Fabrication

2.1 Mirror Design

Three design criteria are employed when designing the proposed DM. First, the desired mode shapes of the DM have to replicate biologically relevant Zernike modes. The human eye exhibits various aberrations that deform incident and reflected light. These aberrations can be represented by Zernike polynomials. Some aberrations correspond to low-order Zernike modes, namely defocus corresponds to mode Z_2^0 Fig. 2.1 (a) and astigmatism corresponds to modes $Z_2^{\pm 2}$ Fig. 2.1 (b). Other aberrations correspond to high-order Zernike modes, such as coma which corresponds to $Z_3^{\pm 1}$, trefoil which corresponds to $Z_3^{\pm 3}$, and tetrafoil which corresponds to $Z_4^{\pm 4}$ [69].

Second, the natural frequencies of those modes should be above the acoustic frequency range $f = 20$ kHz in order to minimize the effects of external disturbances on their response. However, the natural frequencies of the relevant modes should not exceed 100 MHz to avoid complicating the drive circuits required to deliver the actuation voltage.

Finally, the DM is designed to achieve a large 'stroke' for the relevant modes, defined as the transverse distance between the maximum deformation point and the minimum deformation point within one period of oscillations. This criterion is constrained by the fabrication process, Micra-GEM, and limitations on the dimensions of the DM as per the design rules.

The proposed DM is designed to replicate, via dynamic excitation at resonance, six Zernike modes. These modes include low-order and high-order Zernike modes required for opthalmology applications to correct the temporal eye aberrations encountered by scanning

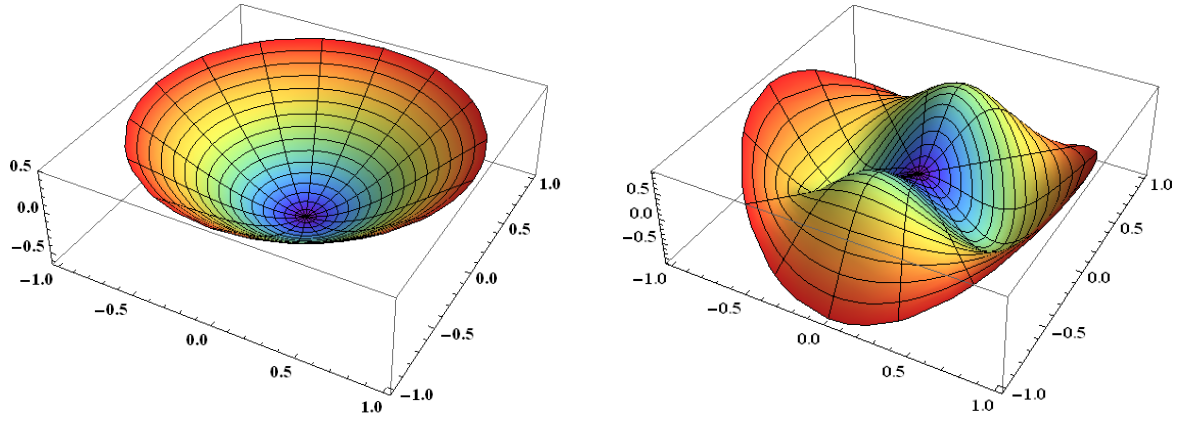

(a) Defocus mode shape Z_2^0 (b) Astigmatism mode shape $Z_2^{\pm 2}$

Figure 2.1: Zernike modes

laser opthalmoscopes (SLO), namely defocus Z_2^0, astigmatism $Z_2^{\pm 2}$, coma $Z_3^{\pm 1}$, trefoil $Z_3^{\pm 3}$, tetrafoil $Z_4^{\pm 4}$, and spherical Z_4^0 modes. Resonant DM has the advantage over the static DM by applying the same voltage to the scheme of electrodes. Therefore, the design reduces the number of fired electrodes that excite a certain mode shape and reduces the complexity of the driving circuits. The complexity of influence function due to mechanical coupling has no longer exist. For example, BMC DM generates the defocus and tetrafoil Zernike modes by firing a 140 electrodes with different voltages depending on its orientation. However, resonant DM generates the defocus and tetrafoil Zernike modes via a 49 and 9 electrodes respectively.

The mirror was designed as a circular plate to match the typical circular shape of wave front aberrations and Zernike modes. It has a diameter of 1.6 mm and a thickness of $10\,\mu m$. Center or mid-span supports were excluded since they impede the continuity of the resulting mode shapes, thereby diverging from Zernike modes. Instead, long and narrow beams were adopted as supports and located at the circumference (edge) of the mirror plate. Further, the beams should be identical and located at equal distances around the mirror circumference in order to create a sectoral symmetry in mirror structure.

In order to determine the appropriate number of support beams, models of the mirror were developed and simulated in COMSOL software using two, three, four, five, six, and seven identical evenly spaced support beams around the mirror circumference. All of them were failed to generate both low and high order Zernike modes. A circular plate supported by eight identical evenly spaced beams was found to allow for the creation

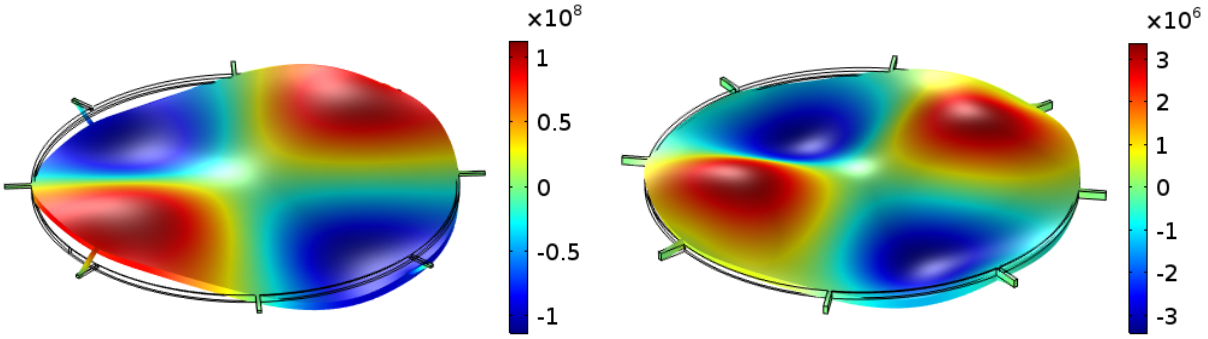

(a) Prototype # 1

(b) Prototype # 2

Figure 2.2: Astigmatism mode for prototype # 1 and prototype # 2

of modes corresponding to the desired Zernike modes. This is the minimum number of support beams that meet the criteria listed above.

The support beams stiffness, and therefore dimensions, can also distort the plate modes away from Zernike modes. COMSOL simulations were carried out to minimize the impact of the support beams on the plate mode shapes and their natural frequencies. The results showed that the support beams stiffness were low enough to minimize their interference with the plate modes when their dimensions were as follows: length l =100 μm, width w =15 μm, and thickness t =10 μm.

For the sake of comparison, two prototypes were fabricated with identical dimensions, except that the beam thickness for prototype # 1 was kept at the recommended design value t =10 μm while the beam thickness for prototype # 2 was increased to 30 μm thickness, Fig. 2.2. The fabrication of the 10 μm thick beams was more challenging when using Micra-GEM. A Y mask was used to etch a 20 μm to create the mirror and the beams. The dimensions and features of the DM are illustrated in Fig. 2.3.

The mirror is electrostatically actuated via 49 concentric electrodes, subdivided into sixteen sectors to match the support system, except for the inner most circle which constituted a single electrode. The electrodes cover the whole area under the mirror plate. The width of the gaps demarcating the electrodes was set to 40 μm to provide for electrical routing within the constraints of the fabrication design rules. The air gap between the mirror and the electrodes was set to 20 μm as per the fabrication constraints. All mirror dimensions for prototype # 1 are listed in Table 2.1.

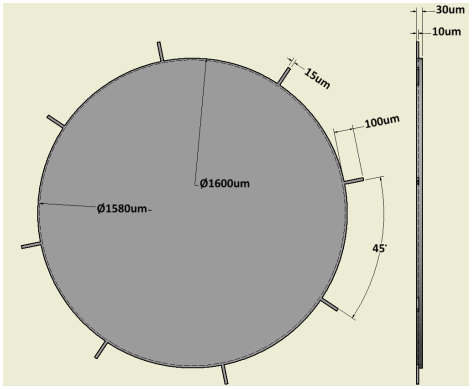

(a) Mirror with 10 μm beam thick

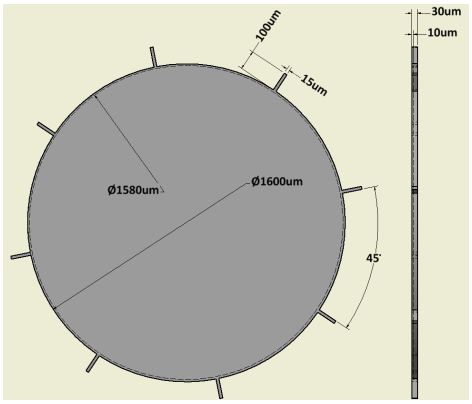

(b) Mirror with 30 μm beam thick

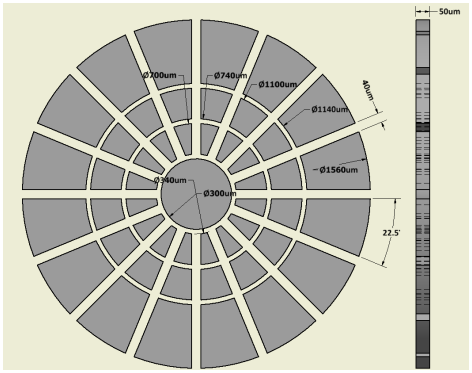

(c) Electrodes configuration

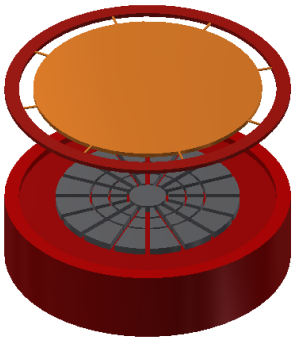

(d) DM structure

Figure 2.3: Mirror dimensions and features

2.2 Mirror Layout and Fabrication

The DM was fabricated based on the Micra-GEM fabrication process [70], which includes two silicon-on-insulator (SOI) wafers, a base (handle) wafer and top (device) wafer. The base wafer was patterned through three deep reactive-ion etching (DRIE) steps, Trench 1, Trench 2, and Trench 3. Mirror plate and support beams were patterned in the top wafer through a single DRIE etch to a depth of 20μm using a Y mask, Fig 2.4[1]. The fabrication process uses five masks to create the mirror and electrodes Table 2.2.

The design layout of the DMs was carried out in the commercial packages MEMS Pro

[1] A permission is shown in Appendix A Fig. A.3

Table 2.1: Dimensions of the DM

Parameter	Prototype # 1 (μm)
Mirror radius, a	*800*
Mirror thickness, t	*10*
Beam length, l	*100*
Beam thickness, h	*10*
Beam width, w	*15*
Capacitive gap, d	*20*

and L-Edit. Prototypes #1 and # 2 were laid out within the design area Fig. 2.5 (a). A microscopic image of the DM is seen in Fig. 2.5 (b).

Table 2.2: Masks of the Micra-GEM fabrication process

Masks	μm
Trench 1	*Etching 51*
Trench 2	*Etching 35*
Y	*Etching 20*
Metal	*Deposition 0.075*
Z	*Etching 30*

The base wafer comprises of a device layer 50 μm thick, a silicon oxide layer 1 μm thick, and a handle substrate 500 μm thick. The top wafer consists of a device layer 30 μm thick, a silicon oxide layer 1 μm thick, and a handle layer 500 μm thick. The DM was fabricated through three processes. First, the electrodes were patterned on the handle layer of the bottom wafer by the Trench 1 mask and a DRIE etch to a depth of 51 μm. Second, a Y mask was used to define the mirror, support beams, and posts in the device layer of the top wafer by etching the mirror plate and beams to a depth of 20 μm. Finally, anodic bonding was applied to connect the two wafers. Wet etching was used to etch away the handle and the silicon oxide layes of the top wafer in order to expose the mirror and support beams. Gold was deposited through a metal mask to create the mirror plate reflective surface. The Z mask was used to etch the whole thickness of the top wafer using DRIE etching and release all features of prototype # 1, Fig. 2.6. The design of prototype # 2 is shown in

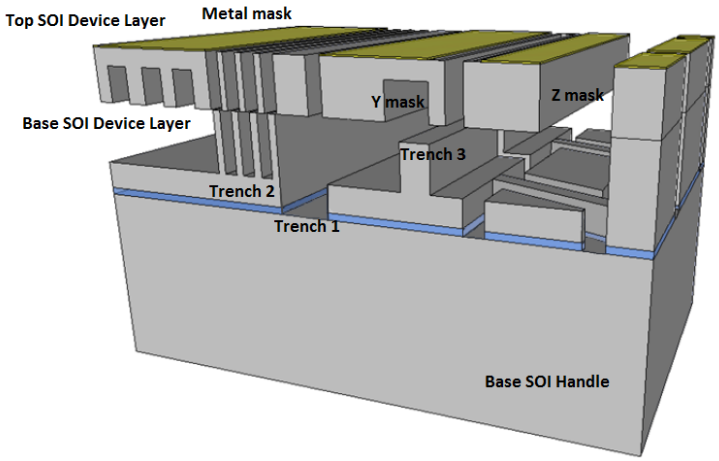

Figure 2.4: Cross-sectional view of Micra-GEM fabrication process

.

Fig. 2.7.

2.3 Modal Analysis

The mirror was made of crystal silicon of a family $< 100 >$ with a modulus of elasticity of $E = 129$ GPa, a Poisson's ratio of $\nu = 0.22$, and a density of $\rho = 2320\,\mathrm{kg/m^3}$. Modal analysis was carried out using the commercial FEM package COMSOL to examine the DM mode shapes and their natural frequencies. The structure was modeled using tetrahedral type with 17307 elements. The FEM results for prototype # 1 showed that mirror modes were exhibited degenerate mode shapes. The frequencies were ordered according to FEM results. The results were replicated low-order Zernike modes which were appeared at $f_1 = 23.8$ kHz for the defocus mode, Fig. 2.8, and $f_4 = 68.23\,\mathrm{kHz}$, and $f_5 = 68.27\,\mathrm{kHz}$ for the astigmatism modes, Fig. 2.9. Spurious (undesirable) modes were appeared at $f_2 = 52.9\,\mathrm{kHz}$, $f_3 = 52.9\,\mathrm{kHz}$, $f_6 = 134.2\,\mathrm{kHz}$, and $f_{12} = 215.39\,\mathrm{kHz}$. The mode shapes corresponding to high-order Zernike modes were appeared at $f_7 = 127.4\,\mathrm{kHz}$ and $f_8 = 127.5\,\mathrm{kHz}$ for the trefoil modes, Fig. 2.10, $f_9 = 136.8\,\mathrm{kHz}$ and $f_{10} = 136.8\,\mathrm{kHz}$, for the coma modes, Fig. 2.11, $f_{11} = 171.6\,\mathrm{kHz}$ and $f_{15} = 286.26$ kHz for the tetrafoil modes, Fig. 2.12, and $f_{16} = 203\,\mathrm{kHz}$ for the spherical mode Z_4^0, Fig. 2.14.

The simulation results showed that two degenerate modes correspond to the astigmatism modes, trefoil, coma, and second astigmatism modes. Selectively exciting one of the

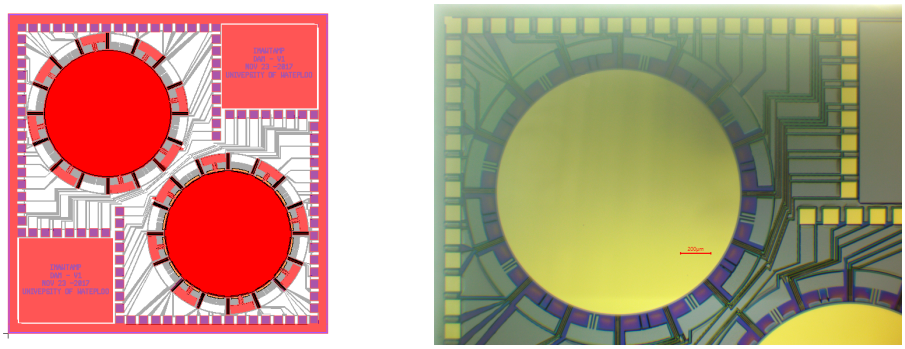

(a) Layout (b) Microscopic image

Figure 2.5: The DM layout

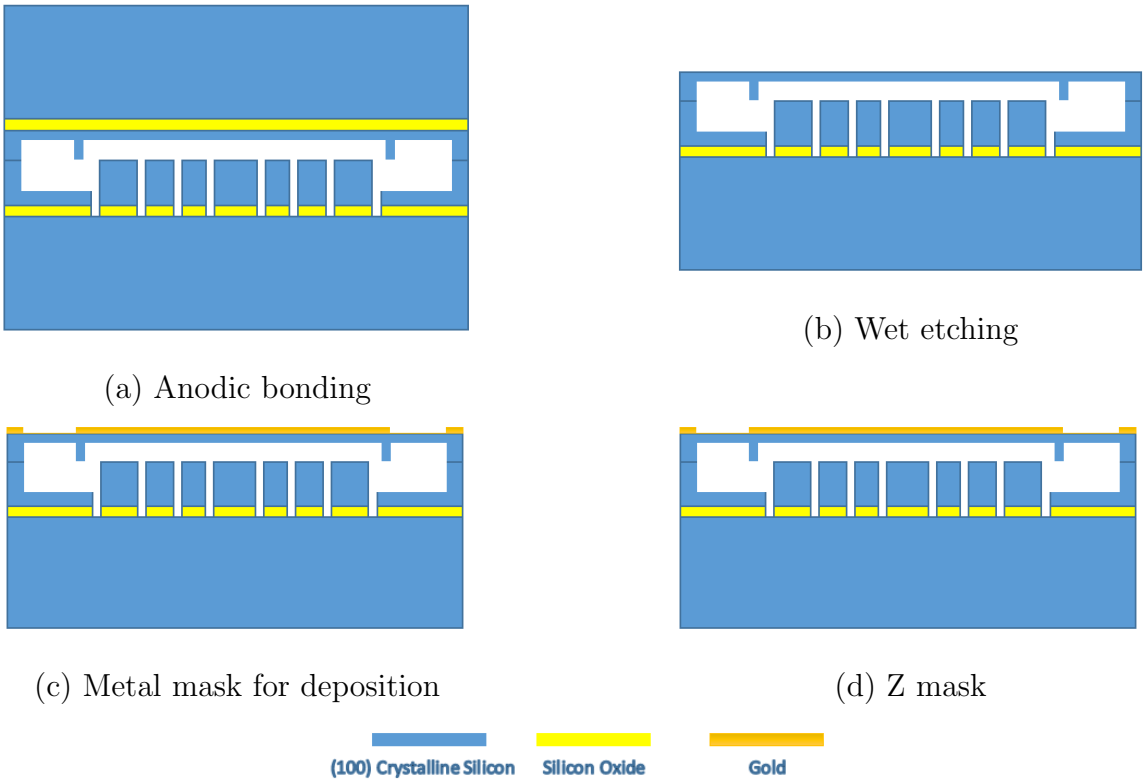

(a) Anodic bonding

(b) Wet etching

(c) Metal mask for deposition

(d) Z mask

Figure 2.6: Final processes

Figure 2.7: A $30\,\mu m$ beam thickness

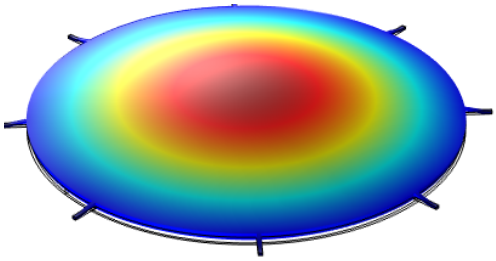

Figure 2.8: The first axisymmetric mode $(1, 0)$ of the mirror corresponding to the defocus mode Z_2^0

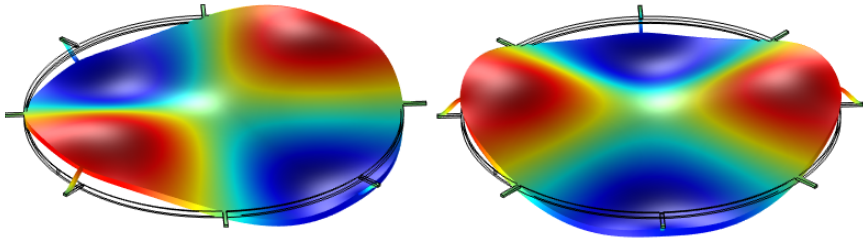

Figure 2.9: The second circumferential modes $(1, 2)$ of the mirror corresponding to the astigmatism modes $Z_2^{\pm 2}$

degenerate modes poses a challenge. The degenerate modes are linearly coupled whenever the difference between their natural frequencies $f_{n+1} - f_n$ is small enough to allow their half-power bandwidths to interfere:

$$\frac{f_{n+1}}{2Q_{n+1}} + \frac{f_n}{2Q_n} \geq f_{n+1} - f_n$$

Nonlinear coupling may further strengthen energy exchange between the modes and result in auto-parametric resonance at higher excitation levels.

Exciting one of the degenerate modes under these conditions will result in complex

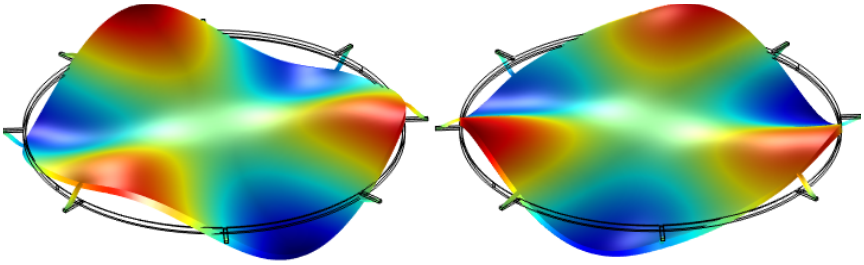

Figure 2.10: The third circumferential modes $(1, 3)$ of the mirror corresponding to the trefoil modes $Z_3^{\pm 3}$

dynamics where the two modes exchange energy. This energy exchange is due to the overlap of two bandwidths. Frequencies lie on the interference area would induce two mode shapes at same frequency. Therefore, it is desirable to develop methods that allow to decouple the degenerate modes, thereby selectively excite each of the degenerate Zernike modes, Z_m^n and Z_m^{-n}, individually.

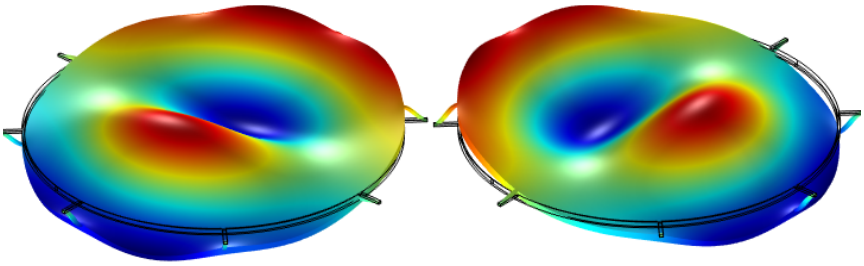

Figure 2.11: The fourth circumferential modes $(2, 1)$ of the mirror corresponding to the coma modes $Z_3^{\pm 1}$

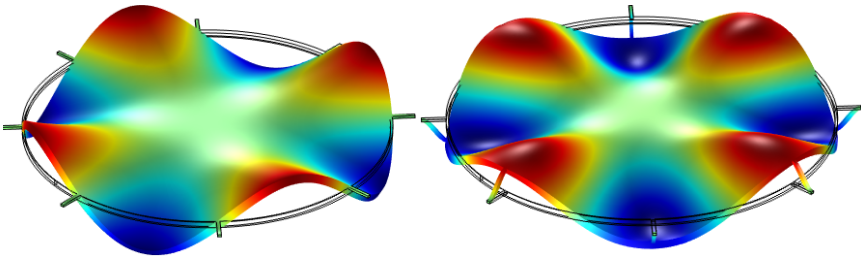

Figure 2.12: The fifth circumferential modes $(1, 4)$ of the mirror corresponding to the tetrafoil modes $Z_4^{\pm 4}$

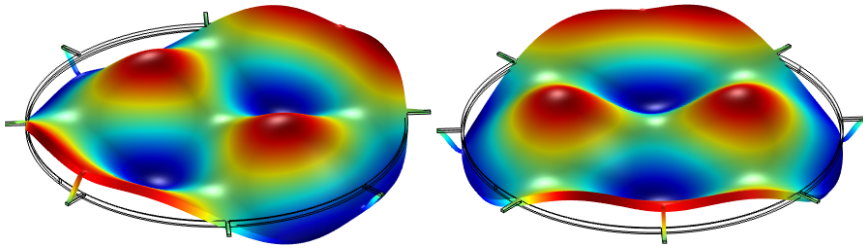

Figure 2.13: The sixth circumferential modes $(2, 2)$ of the mirror corresponding to the second astigmatism modes $Z_4^{\pm 2}$

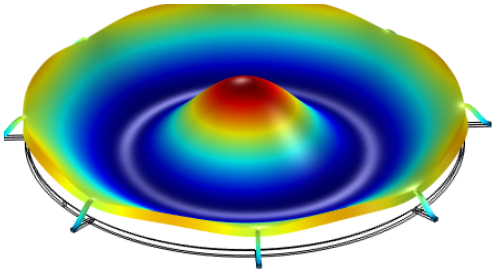

Figure 2.14: The second axisymmetric mode $(2, 0)$ of the mirror corresponding to the spherical mode Z_4^0

2.4 Realization of Degenerate Modes

We found that applying DC voltage selectively to the substrate electrodes can increase the difference between the natural frequencies of the degenerate modes, thus decoupling them. A study of decoupling the degenerate modes was conducted based on extensive numerical simulations of the mirror actuation in COMSOL. Schemes of electrode activations are proposed here for each pair of degenerate modes.

In order to separate the two astigmatism modes, the electrodes between two opposite sectors, out of the four sectors made by the nodal diameter, are activated. This condition was selected to allow the electrostatic field created by those electrodes to approximate the phase relations mandated by the target mode shape on the mirror plate displacement field. To simplify electrostatic actuation, we chose to apply a constant DC voltage to all 'fired' electrodes and to ground the mirror plate. Since the electrostatic force is rectifying, that meant the electrodes were limited to addressing two of the four sectors that were mving in phase. Four actuation schemes that satisfy this condition were tested. The activated electrodes under each scheme are shaded in Fig. 2.15.

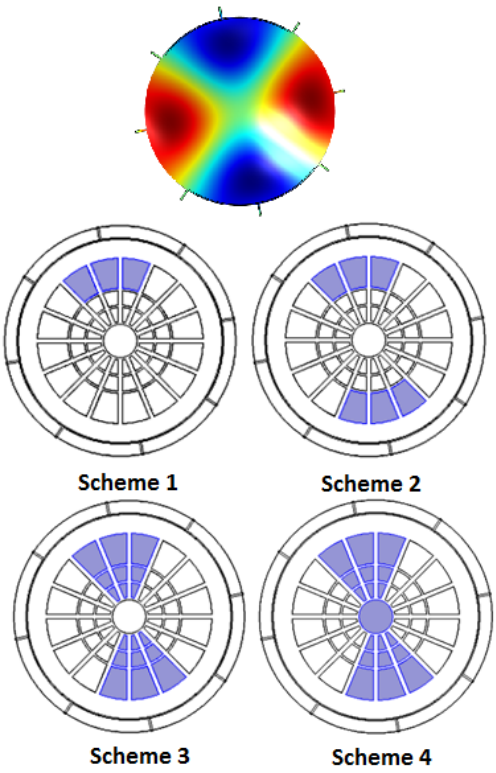

Figure 2.15: Astigmatism actuation schemes

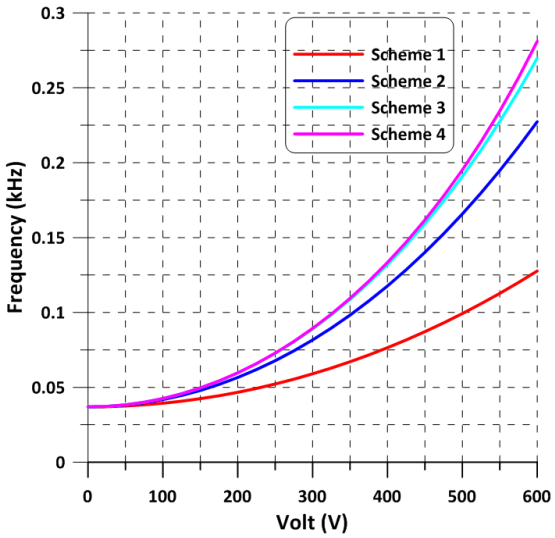

Figure 2.16: Frequency separation between the Astigmatism modes $f_5 - f_4$

Due to the softening effect of the electrostatic force, the natural frequencies of the two degenerate modes, f_4 and f_5, decrease as the DC voltage increases, with the natural frequency of the lower mode f_4 decreasing at a first rate. As a result the frequency difference between the two natural frequencies $f_5 - f_4$ increases under all four actuation schemes as shown in Fig. 2.16. We found that firing the electrodes in one sector only (scheme 1) was not as effective as using the electrodes in two opposite sectors (schemes 2, 3, and 4). Firing the larger tier 4 electrodes combined with the smaller tiers 2 and 3 electrodes were more effective than firing one set only. Scheme 3 was able to increase the separation between the natural frequencies of the two astigmatism modes from 40 Hz to 185 Hz at 500 V. On the other hand, the center (tier 1) had a negligible impact on the degenerate modes. This is expected since both modes have a node over that electrode. As a result, scheme 3 had the most significant effect in decoupling the two degenerate astigmatism mode shapes.

Following the same criteria, three actuation schemes were devised to separate the nat-

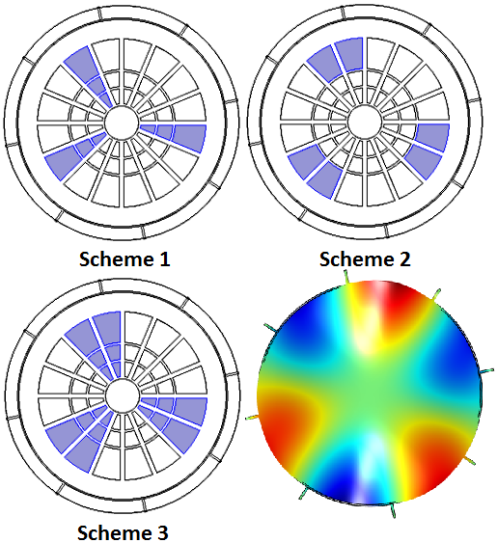

Figure 2.17: Trefoil actuation schemes

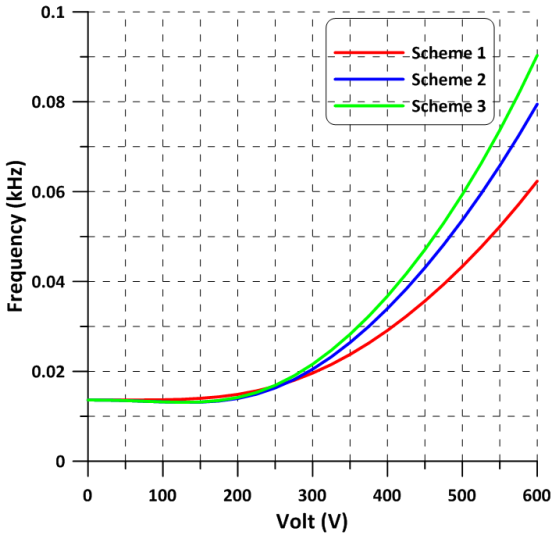

Figure 2.18: Frequency separation between the trefoil modes $f_8 - f_7$

ural frequencies of the two degenerate trefoil modes f_7 and f_8. Scheme 3 fires all tier 2 and 3 electrodes under the plate areas moving in-phase. Scheme 2 fires only tier 4 electrodes under the same in-phase moving areas, while scheme 1 fires only half of these sectors, Fig. 2.17. The difference between the natural frequencies of the degenerate modes $f_8 - f_7$ is shown as a function of DC voltage in Fig. 2.18. Once again, it was found that firing all of tiers 2, 3, and 4 electrodes (scheme 3) was the most effective method in decoupling the degenerate modes increasing the frequency separation from 12 Hz to 60 Hz at 500 V,

In the case of the coma modes, the degenerate modes share a nodal circle. The mirror plate displacement field reverses its direction as it crosses that circle. As a test case, two actuation schemes were devised using tiers 2 and 3 electrodes, which are enclosed within the nodal circle. The actuated fired electrodes in scheme 1 lie on one side of the nodal diameter of the higher mode, shown in Fig. 2.19, while the fired electrodes in scheme 2 are distributed evenly on either side of that nodal line. Figure 2.20 shows the difference between 4 natural frequencies of the degenerate coma modes $f_{12} - f_{11}$ as a function of the DC voltage of the activated electrodes. Scheme 2 was found to be effective in decoupling the two modes, increasing the frequencies separation from a negligible value to 80 Hz at 500 V. On the other hand, scheme 1 was ineffective. The reason for that can be observed in the fact that it reduces the natural frequency of the higher mode to cross that of the lower mode resulting in a negative separation between the two frequencies. Therefore, it is

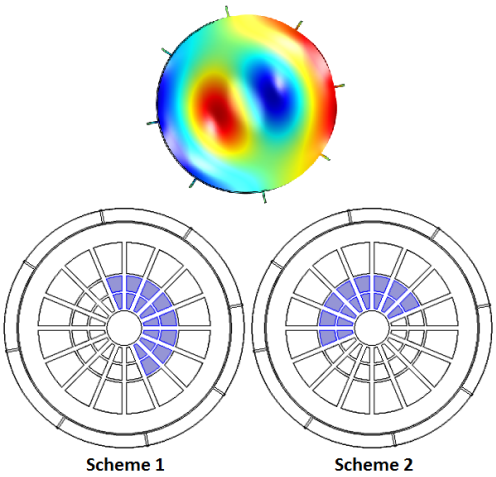

Figure 2.19: Coma actuation schemes

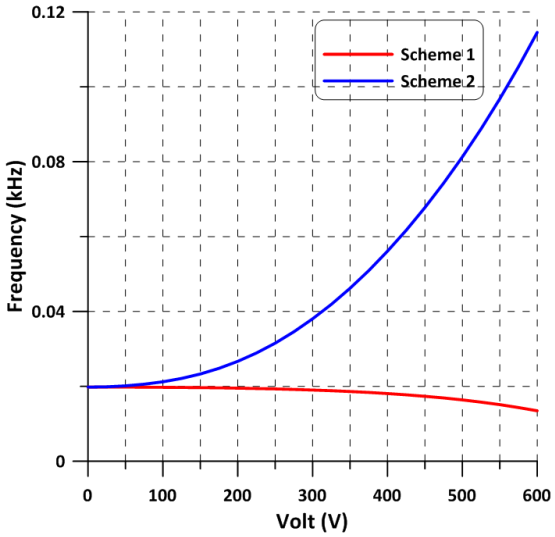

Figure 2.20: Frequency separation between the coma modes $f_{12} - f_{11}$

necessary to target the areas moving in-phase in the lower, rather than the higher, of the two degenerate modes. Using tier 4 electrodes instead of those of tiers 2 and 3 may have even more impact on decoupling the coma modes.

Selective DC actuation of the substrate electrodes can decouple each pair of degenerate modes and reduce the likelihood of their interaction. While the required voltage to realize mode decoupling is high for prototype # 1, it can easily be reduced by redesigning a new mirror with small electrostatic gap distance.

Chapter 3

Pull-in Analysis

3.1 Pull-in voltage

Microplates are used as MEMS devices such as CMUTs (capacitive-micro-machined ultrasound transducers), micropumps, microphones and micromirrors [71, 72, 73, 74]. These microsystems are actuated using eletrostatic, electromagnetic, thermal or piezoelectric excitations. In order to predict the behavior of these microstructures, a mathematical model of a plate equation is solved in order to anticipate the natural frequencies of the structure as well as the mode shapes. The governing equation for the transverse deflection of a circular plate supported by elastic beams $w(r, \theta, t)$ under the electrostatic force is:

$$D\nabla^4 w + \rho h \frac{\partial^2 w}{\partial t^2} = \frac{\epsilon\Big(V_{DC} + V_{AC}\cos\big(\Omega t\big)\Big)^2}{2\big(d-w\big)^2} \tag{3.1}$$

where D is the flexural rigidity

$$D = \frac{Eh^3}{12(1-\nu^2)}$$

E is the Young's Modulus, h is the thickness of the plate, ν is Poisson's ratio, ρ is the density of the material of the mirror, ∇^4 is biharmonic operator, ϵ is the permittivity of the medium which is air, V_{DC} is the applied DC voltage, V_{AC} is the applied AC voltage, Ω is the applied frequency, d is the gap between the mirror and the electrodes. This equation is subject to boundary conditions describing the interface between the mirror

and the support beams around its circumference $r = a$

$$V_r(a, \theta_s) = -k_w\, w(a, \theta_s) \tag{3.2a}$$

$$M_r(a, \theta_s) = k_\phi \left.\frac{\partial w}{\partial r}\right|_{(a,\theta_s)} \tag{3.2b}$$

where a is the mirror plate radius, θ_s are the locations along the mirror plate circumference where the support beams are attached, V_r and M_r are the shear force and bending moment. The lumped translational and rotational stiffnesses of the beams are represented by k_w and k_ϕ.

The mirror plate rigidity D is much higher than that of the support beams EI. In the presence of static loads only, it can be considered as a rigid body and modeled as a lumped mass. Since deflection in the mirror plate is negligible, the term containing the biharmonic operator in the equation of motion Eq.(3.1) approaches zero while the inertia term vanishes identically. The electrostatic force acting on the mirror plate is balanced at its boundaries by the restoring force of the support beams with the shear boundary condition reducing to

$$8k\, w_s = \frac{\epsilon A\, V_{DC}^2}{2\big(d - w_s\big)^2} \tag{3.3}$$

where k is the beam stifness and A is the area of electrodes. For convenience, a non-dimensional variable was derived as the following:

$$\hat{w} = \frac{w}{d} \tag{3.4}$$

Equation(3.3) becomes nondimensionalized as

$$2\, d^3 \left(1 - \hat{w}_s\right) k\, \hat{w}_s = \epsilon A\, V_{DC}^2 \tag{3.5}$$

The stiffness of the support beams acts in parallel to that of the mirror plate. To avoid explicit evaluation of the plate stiffness, we estimate an effective stiffness of each beam that lumps the beam stiffness with the plate stiffness acting as

$$k = \frac{c\, EI}{L^3} \tag{3.6}$$

where c is a correction factor accounting for the parallel configuration of the mirror plate with the beam. The correction factor was calculated from FEM pull-in red curve Fig. 3.1.

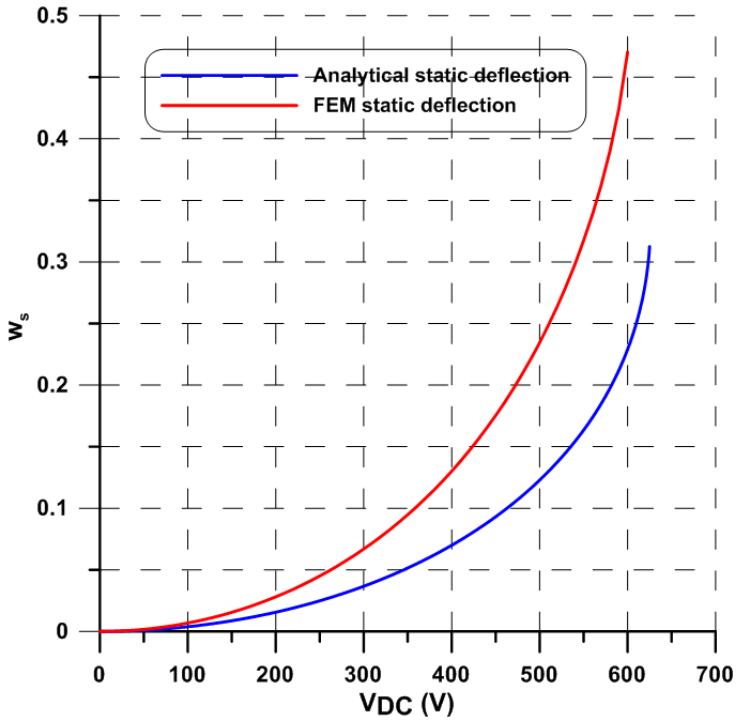

Figure 3.1: Static deflection w_s of the mirror plate as a function of voltage

.

A 600 V pull-in voltage and a 9 um deflection were substituted into Eq.(3.3) from the FEM pull-in curve. The correction factor c was 2.27 and the beam stiffness becomes

$$k = \frac{2.27\,EI}{L^3} \tag{3.7}$$

The new beam stiffness Was substituted back into Eq.(3.5) and eliminate the hat, we get a cubic equation as

$$5882.31\,w^3 - 0.235292\,w^2 + 2.35292 \times 10^{-6}\,w = 1.7794 \times 10^{-17}\,V_{DC}^2 \tag{3.8}$$

Equation (3.8) is a cubic polynomial. It has three solutions, one of them is unphysical corresponding to a displacement larger than the gap between the mirror plate and its electrodes. The other two solutions correspond to physical displacements, corresponding to a smaller stable equilibrium and a larger unstable equilibrium. The two branches of solutions coalesce at the pull-in voltage which is 625 V Fig. 3.2. The corresponding displacement at pull-in is $w_s = 6\,\mu$m. In stable branch, as the voltage increases the displacement increases

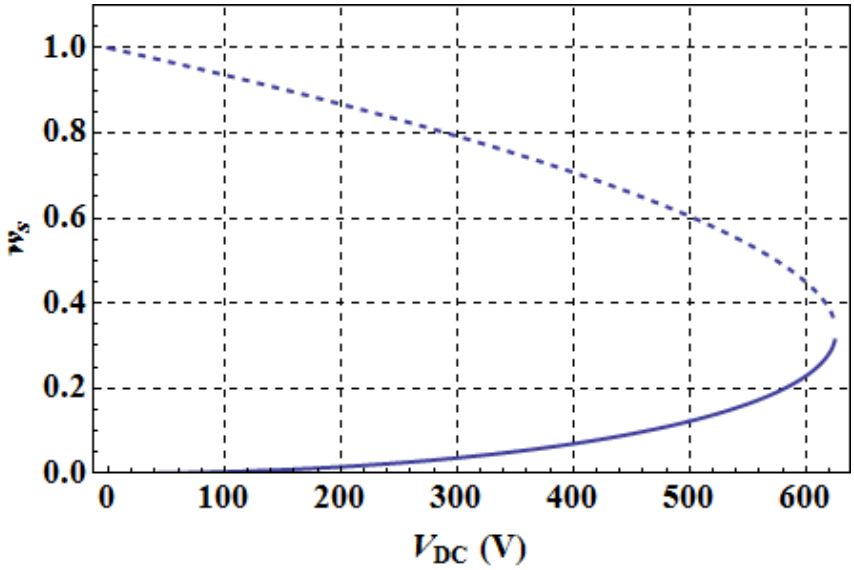

Figure 3.2: Stable (solid line) and unstable (dashed line) equilibria of the mirror plate as functions of voltage

.

to cause failure to the mirror because the mirror plate contact to the electrodes. If any disturbance injects into the mirror, the mirror jumps from the stable to unstable branch and failure (pull-in) occurs.

Chapter 4

Characterization and Experimental Demonstration

4.1 Experimental Setup

A drive circuit was developed to deliver actuation voltage independently to each of the substrate electrodes and to the mirror plate. A schematic of the chip assembly is shown in Fig. 4.1(a). The chip with the two designed DMs was wire bonded to a chip carrier in order to apply voltage to each electrode individually. Each DM was wire bonded individually in a separate chip carrier. The chip carrier is an 84 pin grid array (PGA) with a cavity size of $11.938 \times 11.938\,\text{mm}$, Fig. 4.1(b). The 84 pins of the chip carrier was plugged into a socket

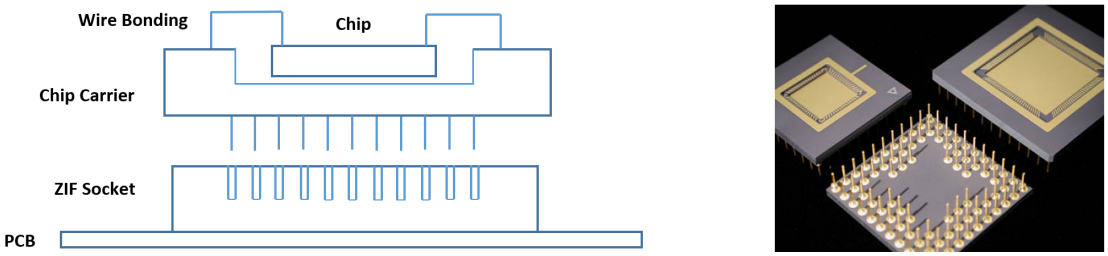

Figure 4.1: (a) A schematic of the chip assembly (b) A picture of the 84 Pin chip carrier .

with 12×12 pin array. The socket was integrated into a printed circuit board (PCB) that has four port slots. Each port was connected to a switch PCB that controls each electrode

individually, Fig. 4.2. Experiments were conducted by placing the PCB carrying the DM and its actuation circuit over the chuck of the vibrometer. The excitation voltage was supplied by a function generator. The response of the DM was detected optically by the reflected laser beam from the DMs surface in order to detect its profile change, Fig. 4.3.

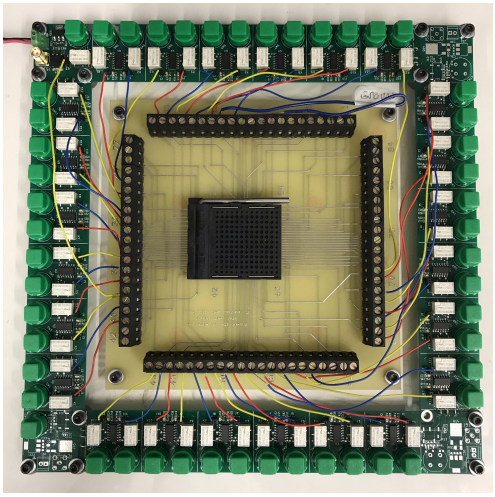

Figure 4.2: The PCB and switching matrix used to address electrodes individually

.

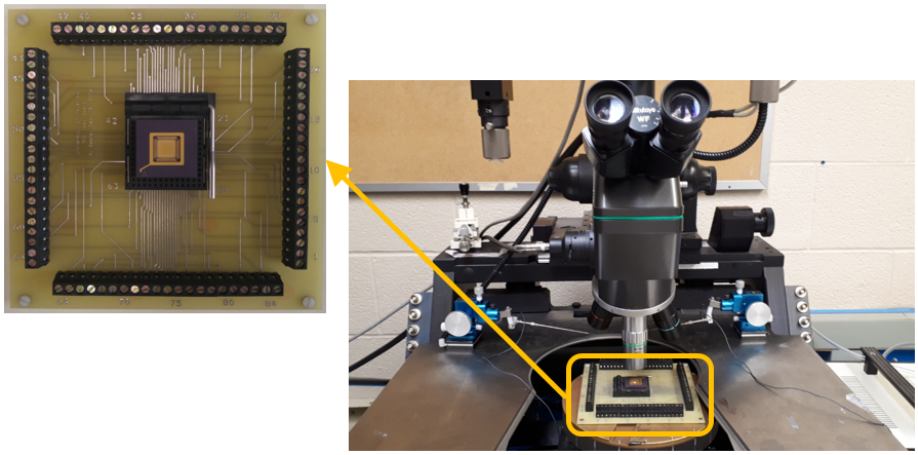

Figure 4.3: Experimental setup of the vibrometer and mirror PCB

.

The setup is comprised of a function generator to generate the excitation signal, a voltage

amplifier to magnify the signal, an oscilloscope to recognize the signal, and Doppler effect laser vibrometer to measure the response. A schematic of the experimental setup is shown in Fig. 4.4.

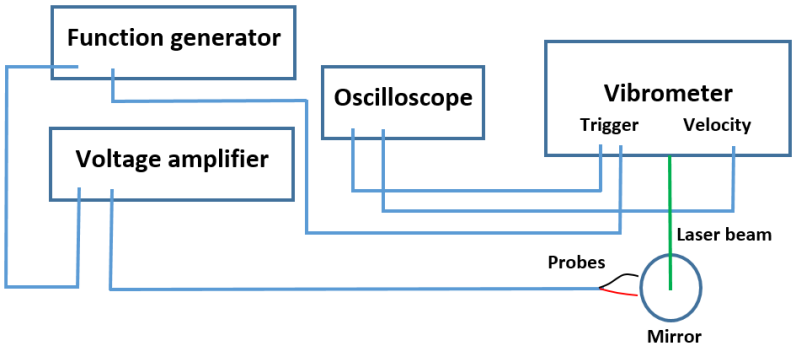

Figure 4.4: Schematic of the experimental setup

.

4.2 Characterization and Experimental Results

The aim of characterization is to find out the resonance frequencies of the mode shapes of the mirror. This was carried out by applying a pulse train Fig. 4.5 at different locations of the mirror surface in order to find out all possible ranges of frequency domains. The quality factor for each mode was estimated from the frequency response curve. A frequency sweep was carried out by applying a constant AC voltage amplitude of 150 volts while changing the frequency in order to plot an accurate frequency response curve. Mode shape corresponds to each resonance frequency was captured by applying a sinusoidal signal with a certain frequency to induce a single mode shape individually. A point-grid was defined to cover the mirror plate surface and a multi-point scan was conducted for each mode separately at each frequency. An analysis of the first axisymmetric mode shape that corresponds to Zernike defocus mode is carried out to calculate the curvature at different phase angle. Validation is examined between the experimental mode shapes and the modeled mode shapes from the FEM analysis.

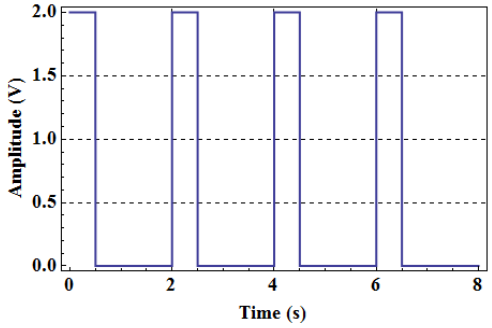

Figure 4.5: A pulse train

.

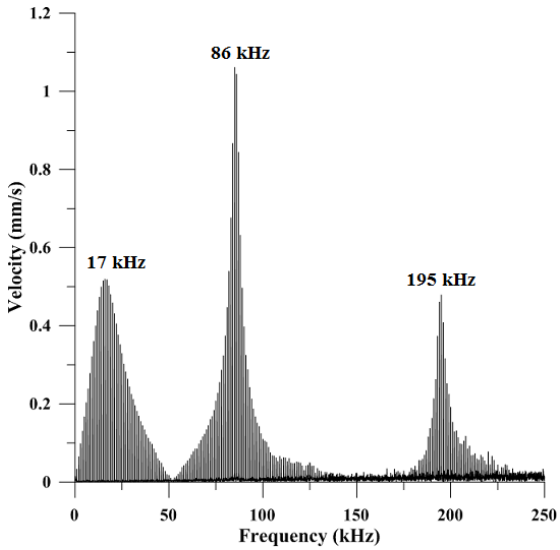

Figure 4.6: Modal response to a pulse train

.

4.2.1 Resonance Characterization

Modal analysis for the DM was conducted using a pulse train of frequency of 1 kHz, an amplitude of 150 volt, and a duty cycle of 0.01. This signal was applied to all electrodes at once. The response of the mirror center was measured using a laser Doppler vibrometer (LDV) which captures the mirror's out-of-plane displacement and velocity at the location of its laser spot. As a result, a modal response shows up with three significant peaks. These peaks showed the first three axisymmetric mode shapes that correspond to the Zernike

axisymmetric modes: defocus, second defocus, and spherical at frequencies 17 kHz, 86 kHz, and 195 kHz respectively, Fig. 4.6. The quality factor for each mode was estimated from the frequency response curve. A frequency sweep was carried out by applying a constant AC voltage amplitude of 150 volts while changing the frequency in order to plot accurate frequency response curves.

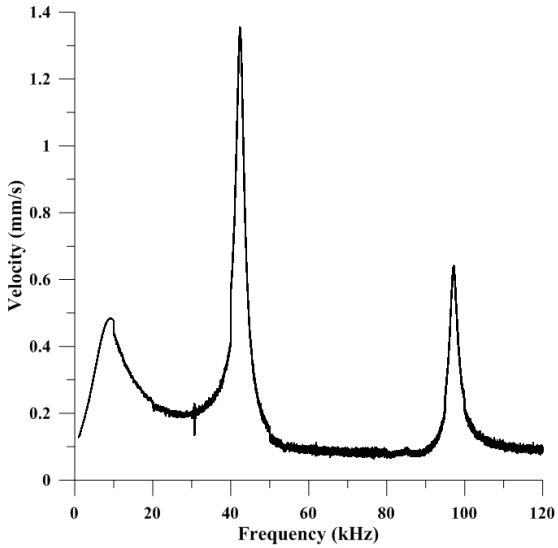

Figure 4.7: Frequency-response curve

.

A frequency sweep was conducted around the three axisymmetric frequencies in order to assure that the resonance occurs at the same values of the modal analysis. This experiment was carried out with a constant voltage amplitude of 150 volts and a frequency change with a step of 1 kHz. The frequency response curve was plotted in Fig. 4.7 and the quality factor of each axisymmetric mode was estimated using the half-power bandwidth technique, where a maximum amplitude is divided by $\sqrt{2}$. The intersection of this height determines the bandwidth that is used to calculate the quality factor as

$$Q = \frac{f_n}{\Delta f} \tag{4.1}$$

The quality factors of the first, second, and the third axisymmetric modes are $Q_1 = 1.3$, $Q_2 = 25$, and $Q_3 = 48$, respectively. The quality factor is the ratio of energy dissipated in one cycle by a resonator to the total energy it stores. The measured values here indicate that the first axisymmetric experiences a much higher rate of energy loss, than the second

and third modes. Free vibrations of the first mode under external disturbances would die down fast with the mirror plate returning to its equilibrium position with two first mode periods $2/f_1 = 0.012\,\text{ms}$.

4.2.2 Mode Shape Characterization

Two sets of modes shapes were accompanied with the circular plates: axisymmetric mode shapes such as defocus and spherical and asymmetric mode shapes such as astigmatism and trefoil. Several grid points on the DM surface were investigated to avoid nodal diameters in asymmetric modes and nodal circles in axisymmetric modes, thereby capturing all modes present in the mirror response. A sinusoidal signal was applied with a certain frequency to induce a single mode shape individually. A point-grid was defined to cover the mirror plate surface and a multi-point scan were conducted for each mode separately at each frequency. In order to induce the first axisymmetric (defocus) mode, a sinusoidal input

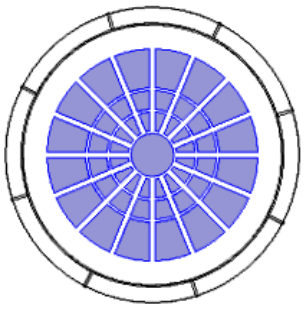

Figure 4.8: The axisymmetric actuation scheme

.

signal was applied to all electrodes at once (the highlighted electrodes are excited with the same voltage) Fig. 4.8. The applied AC voltage signal has a frequency of 8.5 kHz and an amplitude of 150 volts, resulting in an excitation frequency of 17 kHz. The laser beam was located at the center of the mirror so that the response has maximum amplitude, Fig. 4.9(a). Furthermore, a point-grid was defined over the mirror plate, blue square in Fig. 4.9(b), and a multi-point scan were carried out to capture the mode shape it exhibits. To actuate the second axisymmetric mode shape Fig. 4.12, an AC voltage is applied to all electrodes at a frequency of 86 kHz and an amplitude of 150 V. A third axisymmetric mode shape is actuated at 195 kHz and 150 V amplitude Fig. 4.13. This mode shape corresponds to the Zernike spherical mode.

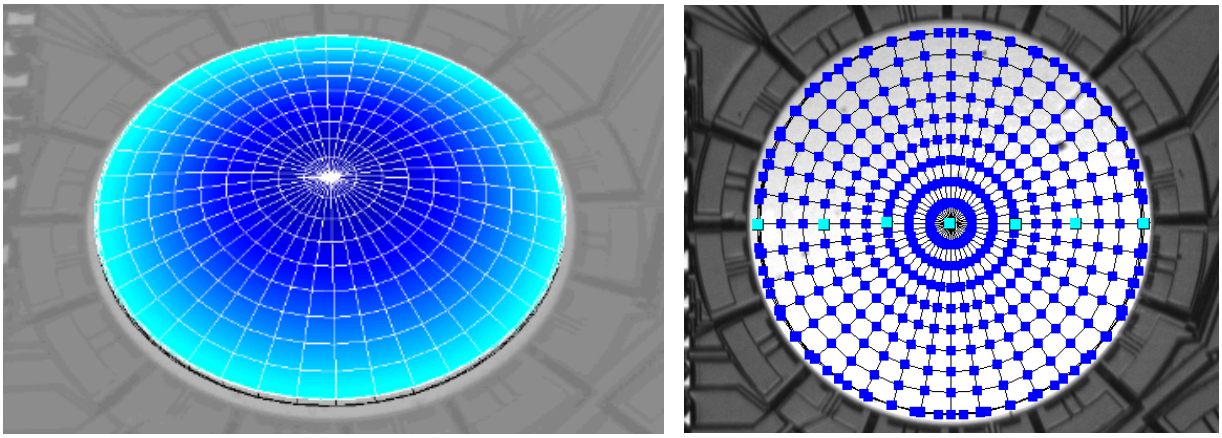

Figure 4.9: (a) The first axisymmetric (defocus) mode shape realized at the excitation frequency $f_{(1,0)} = 17\,\text{kHz}$. (b) The grid points used for measurement along the diameter of the mirror plate

.

In order to capture the circumferential modes, such as astigmatism, coma, trefoil, and tetrafoil, the selective actuation schemes shown in Fig. 4.10 were employed. A modal response is obtained where the laser point is located at the middle of the mirrors radius to avoid the nodal diameters that cross the center of the mirror. However, the circumferential mode shapes are captured at locations where the nodal diameters do not show. The experiments showed that the frequencies 68 kHz, 95 kHz, 123 kHz, and 169 kHz correspond to astigmatism, trefoil, coma, and tetrafoil modes, respectively. In order to capture

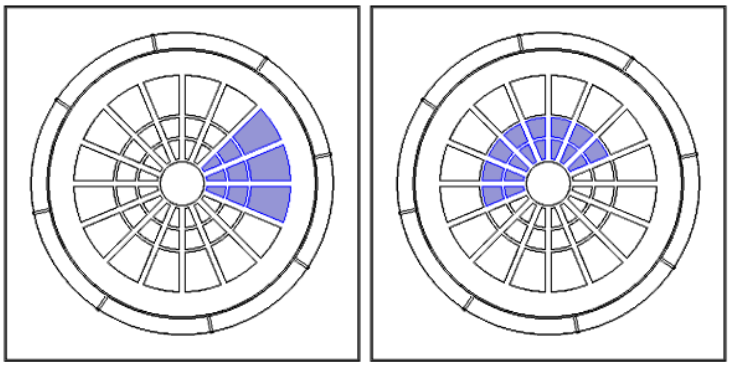

Figure 4.10: Selective circumferential modes

.

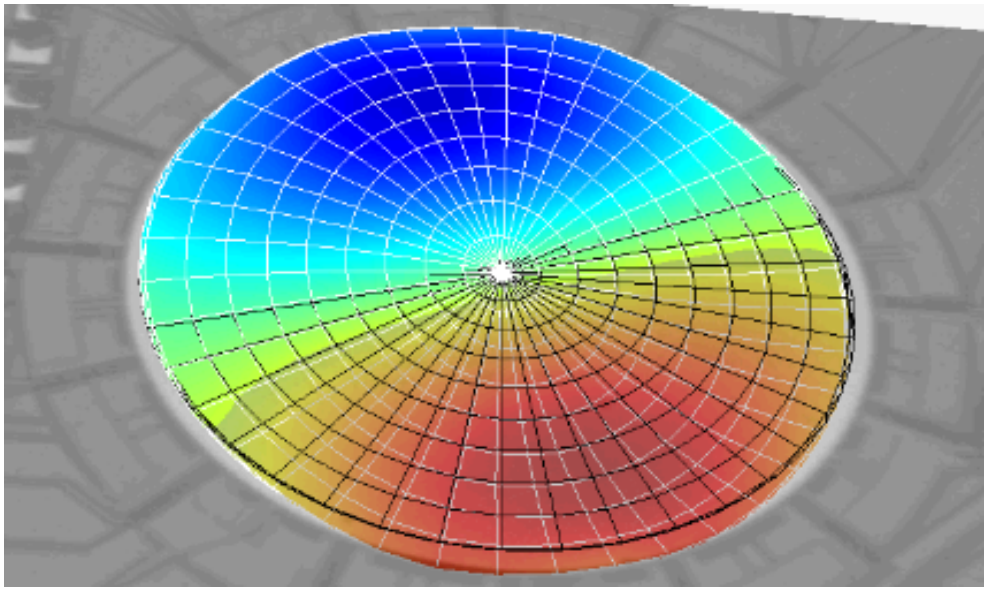

Figure 4.11: The first circumferential mode has a single nodal diameter at $f_{(1,1)} = 43\,\text{kHz}$

.

the individual mode shape, a sinusoidal excitation signal is applied using selective AC actuation schemes at frequencies corresponding to the peak frequency of the mode found in modal response. A multi-point scan is used to capture the modal response of the mirror plate. The first circumferential mode shape, Fig. 4.11 appeared at 43 kHz and 150 volts, where a quarter of the electrodes are fired. At the same electrode scheme, the second circumferential mode shape is shown at 86 kHz frequency and 150 volts, Fig. 4.14. This mode shape approaches the Zernike astigmatism mode Z_2^2.

At frequency of 95 kHz and 150 V amplitude, the third circumferential mode shape which appears corresponds to the Zernike trefoil mode Z_3^{-3}, Fig. 4.15. Finally, at a frequency of 169 kHz and 150 volts, the fourth circumferential mode shape is actuated which corresponds to the Zernike tetrafoil mode Z_4^{-4}, Fig. 4.17. However, different electrodes schemes, as shown in Fig. 4.10, were used to excite the mixed mode shape. This mode shape has one nodal circle and one nodal diameter. In order to excite this mode, a frequency of 123 kHz and a voltage of 150 volts are used. This mixed mode corresponds to the Zernike coma mode, Fig. 4.16.

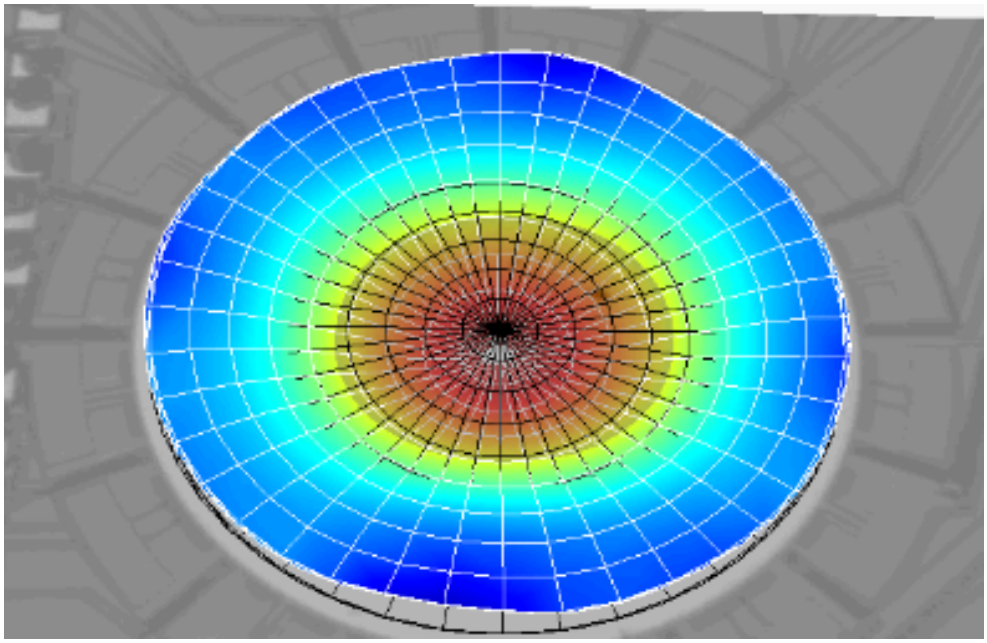

Figure 4.12: The second axisymmetric mode occurs at $f_{(2,0)} = 86\,\text{kHz}$

.

4.2.3 Curvature of the Defocus Mode

The first axisymmetric mode shape can be used to change the focal point of the laser beam. So that the mirror can be used as a variable focal mirror in cameras using this mode. To characterize the evolution of the mirror curvature over the phase angles of the first axisymmetric mode, we measured the mirror displacement at a set of nine grid points along the mirror diameter to the end of the beam, shown in cyan in Fig. 4.9(b). Those points were located along an x-axis with origin at the mirror center at: -900, -756, -504, -252, 0, 252, 504, 756, 900 um. The displacement time-history was measured at each of those points as shown in Fig. 4.18(a) for the center point ($x = 0$). At each point, the displacement time-record over multiple cycles was transformed to phase-angle to obtain the displacement-phase angle plot shown in Fig. 4.18(b) for the center point ($x = 0$). The average displacement over these cycles were calculated for a set of phase angles. The average displacements for the center point ($x = 0$) are listed in Table 4.1. The average displacements of the seven diameteral grid points are shown in Fig. 4.19 as functions of their position along the diameter (normalized with respect to the mirror radius) for a set of 18 constant phase angles from 90^o to 270^o in steps of 10^o.

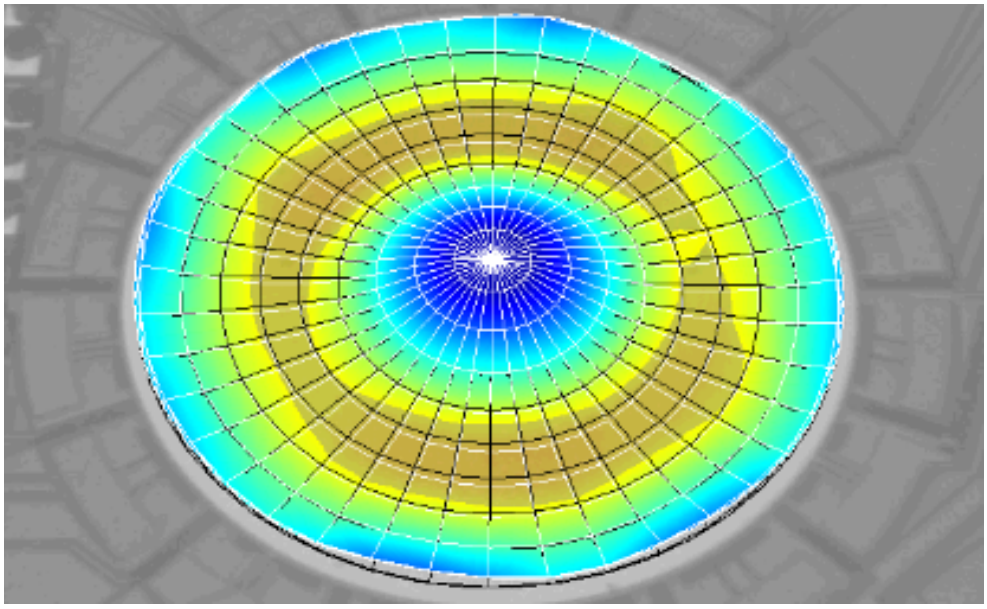

Figure 4.13: The third axisymmetric mode occurs at $f_{(3,0)} = 195\,\mathrm{kHz}$

.

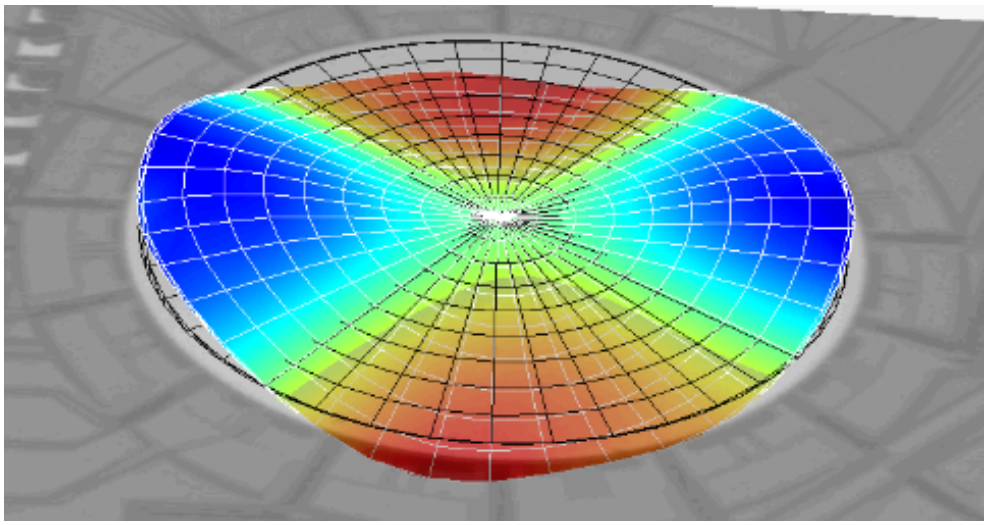

Figure 4.14: The second circumferential mode with two nodal diameters corresponds to astigmatism at $f_{(1,2)} = 68\,\mathrm{kHz}$

.

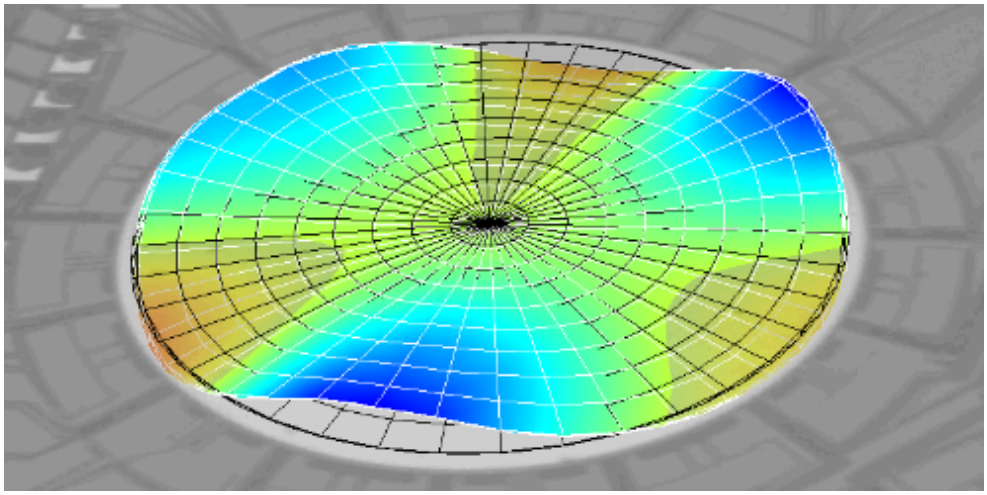

Figure 4.15: The third circumferential mode with three nodal diameters corresponds to trefoil at $f_{(1,3)} = 95\,\text{kHz}$

.

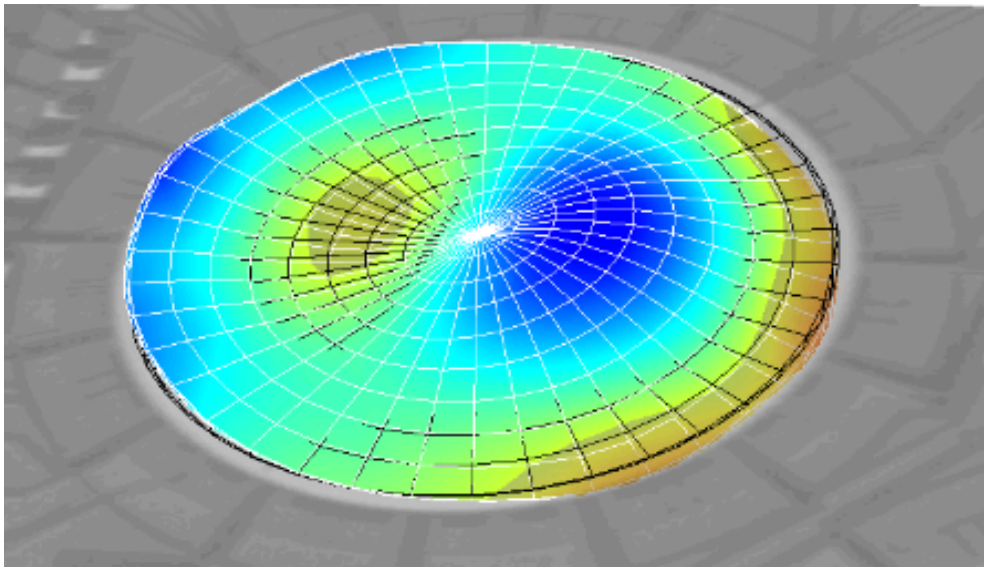

Figure 4.16: The fourth circumferential mode with single nodal diameter and single nodal circle corresponds to coma at $f_{(2,1)} = 123\,\text{kHz}$

.

The measured displacements at the same phase angle were used to estimate the mirror

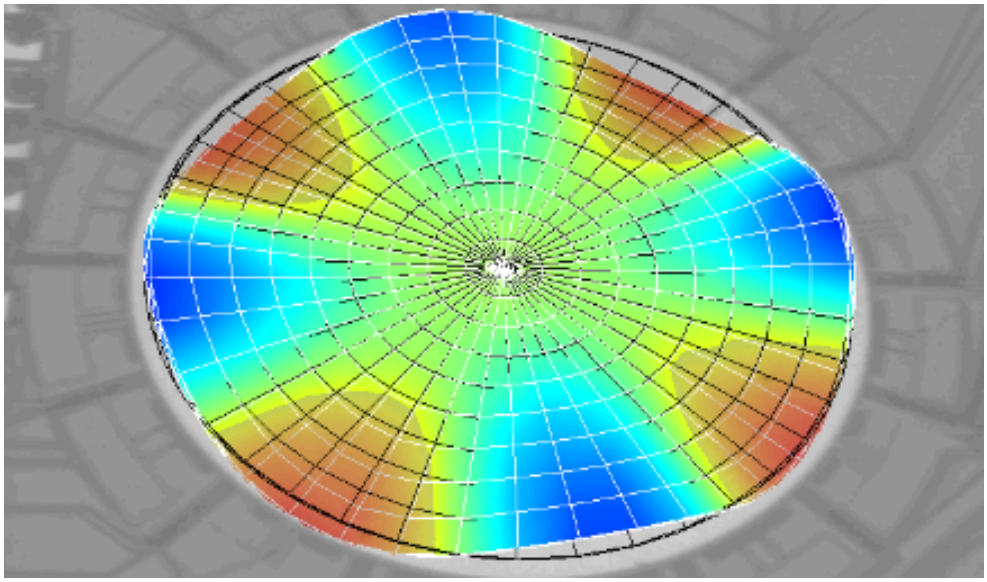

Figure 4.17: The fifth circumferential mode with four nodal diameters corresponds to tetrafoil at $f_{(1,4)} = 169\,\text{kHz}$

.

Table 4.1: Displacement of the mirror center as a function of phase angle

Phase Angle ϕ	90^o	110^o	130^o	150^o	170^o	190^o	210^o	230^o	250^o	270^o
Average displacement (nm)	420.78	395.42	325.49	214.02	80.33	-62.87	-200.49	-318.30	-393.97	-421.46

curvature at that phase. Towards that end, a least square fit was deployed to approximate the deflection of the mirror plate at a given phase angle ϕ as a fourth-order function of the diameteral position r:

$$w^{\phi}(r) = a + b\,r^2 + c\,r^4 \tag{4.2}$$

where a, b, c are the coefficients of obtained from the fit. The deflection was obtained for each of the phase angles listed above. For example, the deflection of the defocus mode at a phase angle of $\phi = 90°$ was found to be:

$$w^{90}(r) = 0.988784 - 1.10374\,r^2 + 0.11762\,r^4 \tag{4.3}$$

The radius of curvature for each phase angle is then calculated from the relationship

$$\rho^{\phi}\big(r\big) = \frac{\left[1 + \left(\frac{dw^{\phi}}{dr}\right)^2\right]^{\frac{3}{2}}}{\frac{d^2w^{\phi}}{dr^2}} \tag{4.4}$$

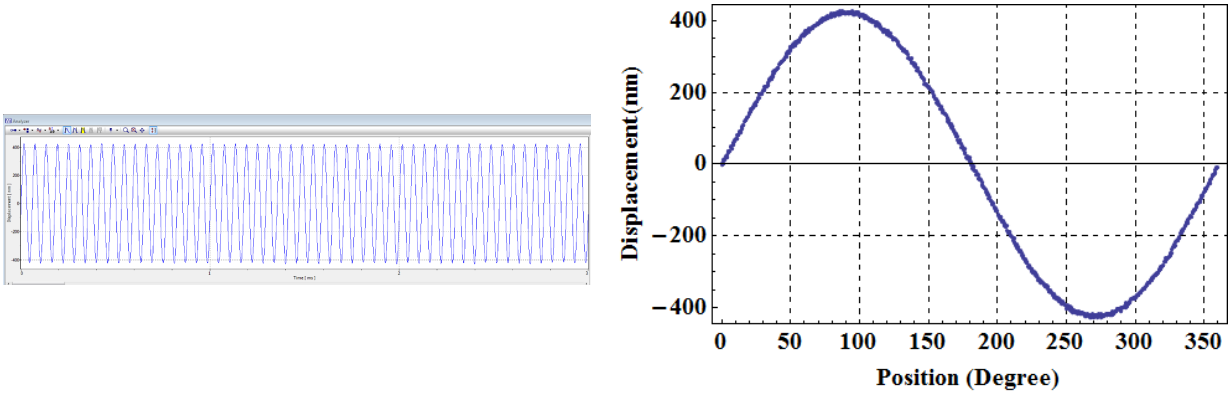

Figure 4.18: (a) Displacement time-history. (b) Displacement versus phase angle.

.

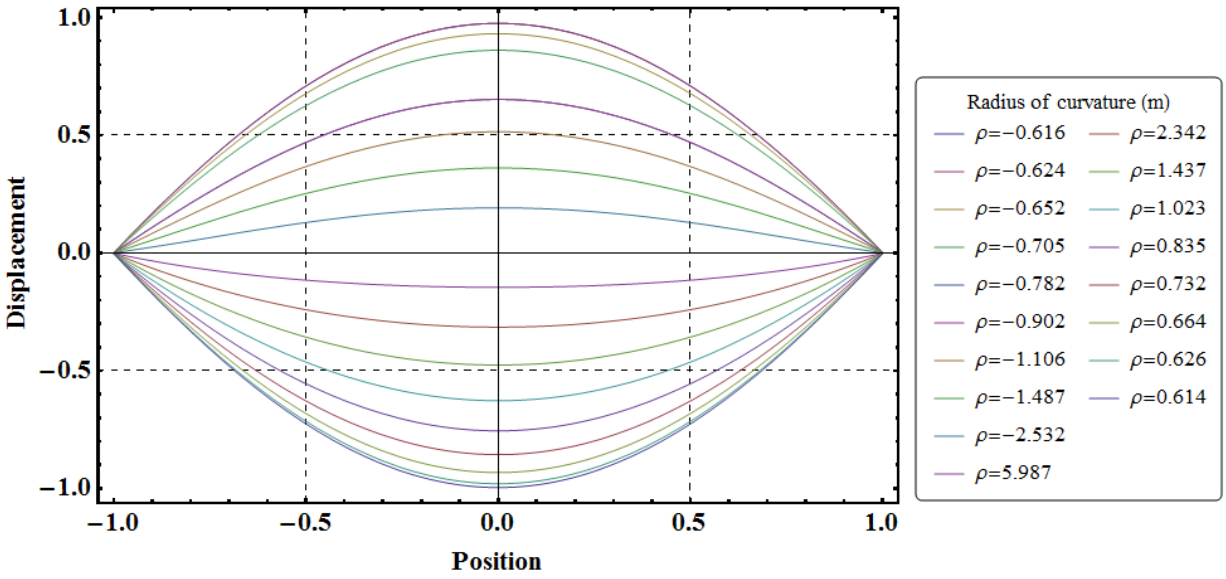

Figure 4.19: Radius of curvature of the first axisymmetric (defocus) mode of vibrations

.

Table 4.2 lists the phase angle and the corresponding radius of curvature at the plate center $\rho^{\phi}(0)$. For example, at a phase angle of 90^{o}, the radius of curvature is 0.616 m. The aim of this work was the design of a resonant DM that can replicate the Zernike modes with the least number of electrodes actuated using the same voltage. This is in contrast to static DM with their influence functions which require different actuation voltages applied to a large number of electrodes.

Table 4.2: Radius of curvature as a function of phase angle

Phase angle $\phi\,(^o)$	90	100	120	140	160	190	200	220	240	270
Radius of curvature (m)	-0.959	0.970	-1.095	-1.438	-2.548	7.215	3.169	1.539	1.115	0.951

In order to evaluate the accuracy of the generated modes, the differences among three mode shapes were evaluated: the ideal Zernike defocus mode, the FEM defocus mode, and the measured first axisymmetric mode. First, we examined whether the simulated mode was axisymmetric. Towards that end, two sets of nine grid points were defined along two radii of the FEM model. One set of points along a radius aligned with the beam center-line. Another set of points along a radius mid-way between two adjacent beams as shown in Fig. 4.20.

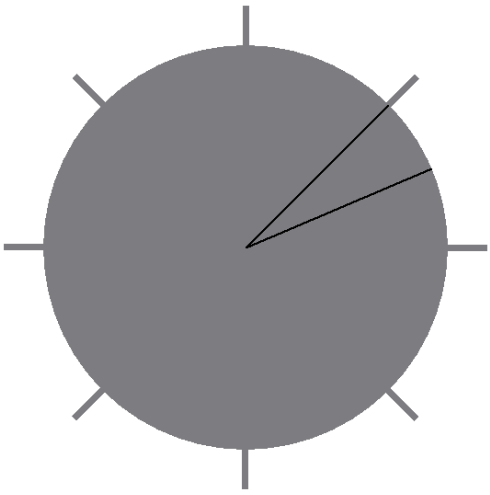

Figure 4.20: Radii at beam attachment and free end

.

The displacement along these points were obtained from Comsol when the mode shape was at a phase angle of $\phi = 90°$. A comparison of the deflection between the two radii was carried as shown in Fig. 4.21. It was found that the deflection along the two radii was almost identical except for the last point at the edge of the mirror plate. Since those radii correspond to the maximum and minimum compliance lines along the plate, it is reasonable to assume that the mode shape is axisymmetric. Therefore, a function representing the defocus mode from the FEM model can be found following the procedure described above for the experimental mode shape:

$$w_{\text{FEM}}(r) = 0.542484 - 1.53369\,r^2 + 0.542484\,r^4 \tag{4.5}$$

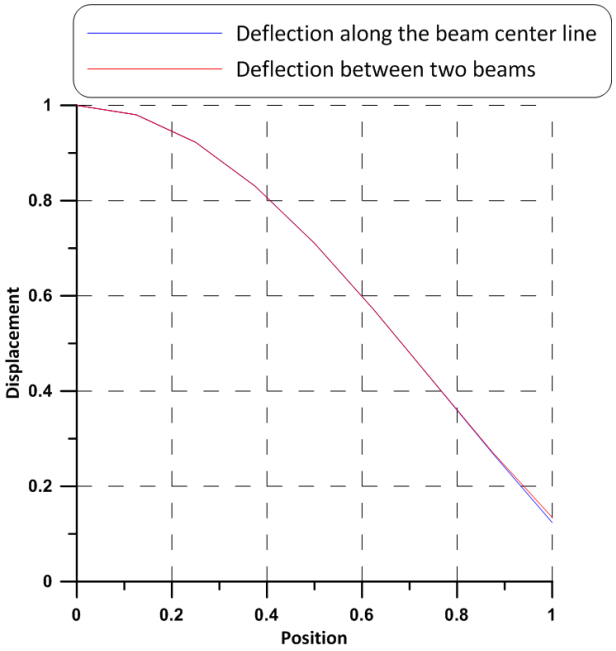

Figure 4.21: Comparison of deflection along a beam center-line to that along a radius mid-way between two beams

.

The displacements and the distances along the mirror radius were normalized by dividing both measurements by its maximum value for all three modes and are shown in Fig. 4.22. The difference between the FEM simulation and experimentally realized defocus modes and the normalized Zernike defocus mode ($Z_2^0(r) = 1 - r^2$) was determined as the difference between the modes averaged over the plate area

$$e^2 = \frac{1}{A}\int_0^{2\pi}\int_0^1 (Z_2^0(r) - w(r))^2 r dr d\theta \tag{4.6}$$

where $w(r)$ is the simulated and experimental modes: $w_{FEM}(r)$ and $w_{exp}(r)$, respectively, and the normalized plate area is $A = \pi$. The deviation of the simulated and experimental modes from the ideal Zernike mode at $\phi = 90°$ was found as the square root of that quantity: $e = 23$ and 6 nm, respectively. Comparing the last value to the maximum deflection of the experimental mode shape, 420 nm, indicates that its deviation from the Zernike defocus mode is less than 1.5%. We note that a deviation of 6 nm from the ideal mode is compared with those for continuous DM in the literature which varies in the range 1.8 to 7.6 nm [23]. We also note that these results were obtained without any need for close-loop control or

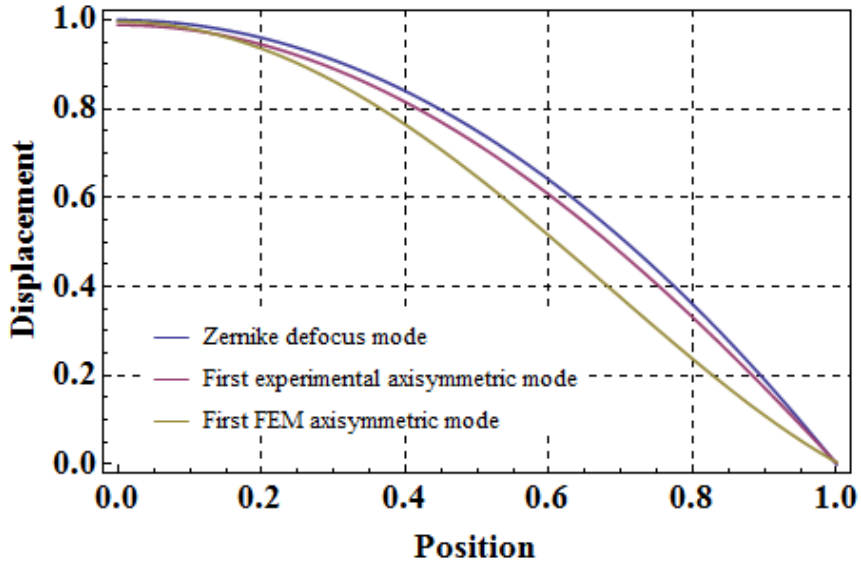

Figure 4.22: The normalized profiles of the Zernike, experimental, and FEM defocus modes along a mirror radius

.

actuation involving the distribution of multiple voltage levels to different electrodes which further emphasize the promise of resonant adaptive mirrors.

The two-dimensional profiles of the normalized experimental and simulated defocus mode shapes are represented as bodies of revolution and compared to the ideal three-dimensional Zernike defocus mode in Fig. 4.23.

4.3 Validation of Experimental Results

A comparison between the experiments and the numerical analysis was addressed in Table 4.3. The experimental first axisymmetic mode shape had an excitation frequency of 17 kHz, while the FEM first axisymmetric mode shape of 23.8 kHz with a frequency difference of 6.8 kHz. An exactly match between the experimental and FEM astigmatism mode shape with a frequency of 68 kHz. The frequency of the experimental trefoil mode had a deviation of 12.5 kHz from the FEM trefoil frequency. Another deviation was appeared of 13.8 kHz frequency between the experimental and FEM coma mode shape. A small deviation between the experimental and FEM tetrafoil and spherical mode shapes of 2.6 kHz and 4 kHz frequency respectively.

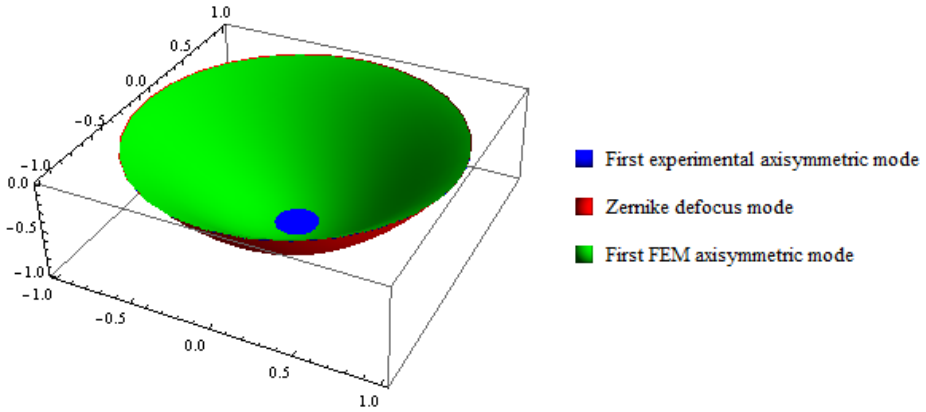

Figure 4.23: The normalized Zernike, experimental, and FEM defocus modes

.

Table 4.3: Displacement measurements of center grid point

	Defocus	Astigmatism	Trefoil	Coma	Tetrafoil	Spherical
Experiments (kHz)	17	68	95	123	169	195
FEM (kHz)	23.8	68.23	127.5	136.8	171.6	203

4.4 Electromagnetic actuation of the DM

Another actuation mechanism was proposed using electromagnetic actuation technique to excite the DM. The aim of this technique is to reduce the voltage that was used in electrostatic actuation. In order to establish the required strength of the magnetic field for excitations, two magnets were chosen with appropriate dimensions of 6.35 mm length, 3.175 mm width, and 0.793 mm thickness. These magnets were placed in the cavity of the chip carrier in order to produce a permanent magnetic field. A small AC potential difference was applied to two aligned mirror's beams using two probes in order to pass current. So that the magnetic field was perpendicular to the current direction. As a result, a Lorentz force was actuated the mirror plate in a direction that was perpendicular to its plane Eq.(4.7). The force exerted uniform deflection at the mirror profile as the magnetic field uniformly distributed by perfectly aligning the magnets. An AC voltage was applied to excite the DM to its natural frequency that generate the Zernike modes. The current path length was approximated by the diameter of the mirror and the length of two beams in which the probes were attached.

$$\vec{\mathbf{F}} = \ell \ \vec{\mathbf{i}}(t) \times \vec{\mathbf{B}} \tag{4.7}$$

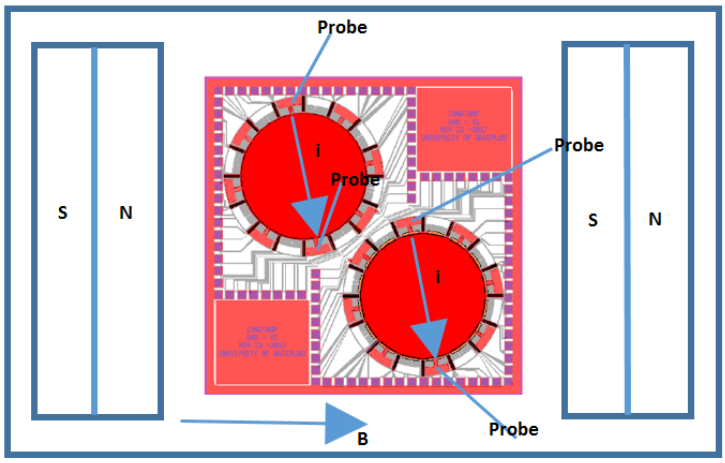

Figure 4.24: Electro-magnetic actuation of the DM

.

where $\vec{\mathbf{F}}$ is the Lorentz force, l is the length of the conductor, $\vec{\mathbf{i}}(t)$ is the electric current, and $\vec{\mathbf{B}}$ is the magnetic field. An initial test of using the electromagnetic actuation was conducted using an AC voltage signal that has a frequency of 8.5 kHz and a maximum amplitude of 60 volts in order to induce the first axisymmetric mode shape. The result showed two responses: first response at frequency of 8.5 kHz due to electromagnetic actuation, and second response at 17 kHz due to electrostatic actuation that induced implicitly. The first axisymmetric mode shape that replicate the Zernike defocus mode was occurred at one of the two frequencies. In order to recognize this mode at 17 kHz, a sinusoidal signal of a frequency 8.5 kHz, and an amplitude of 60 V was applied using two probes to the electrodes and the mirror plate. This signal eliminated the response at 8 kHz and the mode shape was captured at 17 kHz Fig 4.25.

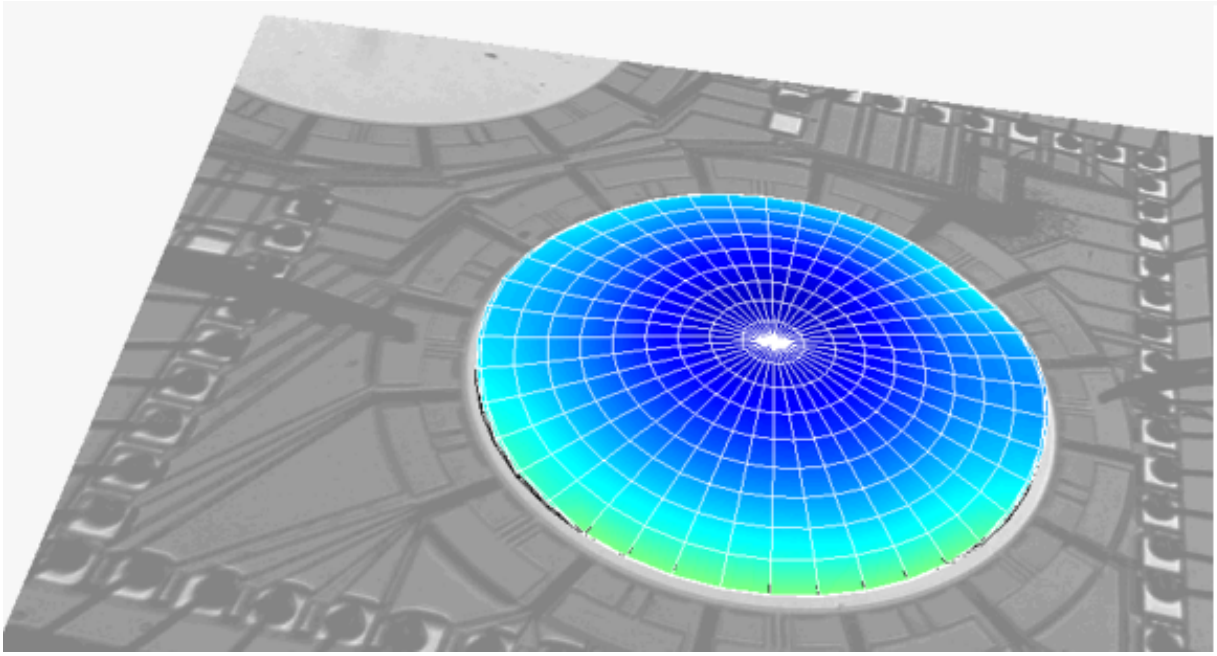

Figure 4.25: The first axisymmetric mode occurs at $f_{(1,0)} = 17\,\mathrm{kHz}$

.

Chapter 5

Conclusions and Future Work

Circular continuous MEMS DMs were designed and fabricated to detect and correct human eye's wavefront aberration. The MEMS DMs were designed using FEM COMSOL software. The DMs were fabricated using the Micra-GEM micro-fabrication process. Human eye's wavefront aberration are represented by a set of Zernike modes. Therefore, three design criteria were considered to meet the desired Zernike modes that are utilized in ophthalmic application. The resonant DMs allow the elimination of the spatial control and exploiting the amplification factor. The number, shape, and arrangements of the excitation electrodes were optimized to excite the mode shapes that match the required set of Zernike modes leading a significant reduction in the complexity of the hardware required for mirror excitation. This reduction is in terms of reducing the number of electrodes that is used to excite certain mode shape. Additionally, resonant DMs eliminate the use of applying different voltage schemes to generate Zernike modes and it replace them by only one elctrode scheme with same voltage. For example, a 140 electrodes of a MEMS DMs were used with different voltage values to generate the astigmatism mode while the resonant DMs was applied same voltage value to a nine electrode to excite the same mode. Therefore, a significant reduction in the electrical and control circuits was carried out using the resonant DMs.

The experimental results show that the measured mode shapes replicate the desired Zernike modes. The first axisymmetric mode shape that corresponds to the defocus mode has a stroke of 800 nm which is a sufficient to correct for the laser beam of wavelengths up to 800 nm such as Ion argon 488 nm and He-Ne 632.8 nm. The RMS error between the first axisymmetric mode of the resonant DMs and the the Zernike defocus mode is 6 nm. This RMS error was achieved by the least number of electrodes with the same voltage and without using a complex electrical circuits and control units. However, static DMs achieve

a value of RMS error of range 1.8-7.6 nm using complex electrical and control circuits. The resonant DMs propose a new technique that replace the continuous laser scanning by a pulsed laser scanning of the human eye. The highest image resolution of the retina will be captured at the maximum amplitude of the DMs. The challenge is to synchronize the frequency of the pulsed laser scanning with the frequency of each mode corresponding to Zernike mode. High speed camera will be used to capture the image at maximum amplitude of the DM. For future work, the proposed scheme will be implemented in order to separate the degenerate mode shapes. The splitting action will be obtained by applying a DC voltage to certain schemes of electrodes. Characterization will be conducted using the vibrometer to measure the degenerate modes and evaluate each mode individually. Testing the efficacy of the proposed DM with an optical setup to examine the image resolution is for future work

References

[1] G. M. Dai, *Wavefront optics for vision correction*, vol. 179. SPIE press Bellingham, 2008.

[2] J. C. López, A. B. Díaz, O. T. Rojas, and Y. T. Moreno, "Atmospheric turbulence temperature on the laser wavefront properties," in *Journal of Physics: Conference Series*, vol. 850, p. 012001, IOP Publishing, 2017.

[3] J. Schwiegerling, "Field guide to visual and ophthalmic optics," SPIE, 2004.

[4] "Environment, health, and safety division." http://www2.lbl.gov/ehs/safety/lasers/bioeffects.shtml. Accessed: 2018-07-10.

[5] "Mems based deformable mirrors." https://www.thorlabs.com/newgrouppage9.cfm?objectgroup_id=3258. Accessed: 2018-07-10.

[6] J. A. Kubby, *Adaptive Optics for Biological Imaging*. CRC press, 2013.

[7] B. M. Corporation, "Adaptive Optics 101," tech. rep., Boston Micromachines Corporation, 09 2014.

[8] B. M. Corporation, "Hex Class Deformable Mirrors," tech. rep., Boston Micrmachines Corporation, 09 2014.

[9] V. Lakshminarayanan and A. Fleck, "Zernike polynomials: a guide," *Journal of Modern Optics*, vol. 58, no. 7, pp. 545–561, 2011.

[10] J. B. Stewart, T. G. Bifano, S. Cornelissen, P. Bierden, B. M. Levine, and T. Cook, "Design and development of a 331-segment tip–tilt–piston mirror array for space-based adaptive optics," *Sensors and Actuators A: Physical*, vol. 138, no. 1, pp. 230–238, 2007.

[11] N. Doble, G. Yoon, L. Chen, P. Bierden, B. Singer, S. Olivier, and D. R. Williams, "Use of a microelectromechanical mirror for adaptive optics in the human eye," *Optics letters*, vol. 27, no. 17, pp. 1537–1539, 2002.

[12] S. Manzanera, M. A. Helmbrecht, C. J. Kempf, and A. Roorda, "Mems segmented-based adaptive optics scanning laser ophthalmoscope," *Biomedical optics express*, vol. 2, no. 5, pp. 1204–1217, 2011.

[13] G. N. Rodrigues, R. P. Bastaits, S. Roose, Y. Stockman, S. E. Gebhardt, A. J. Schönecker, P. Villon, and A. J. Preumont, "Modular bimorph mirrors for adaptive optics," *Optical Engineering*, vol. 48, no. 3, p. 034001, 2009.

[14] S. A. Cornelissen, P. A. Bierden, T. G. Bifano, and C. L. V. Lam, "4096-element continuous face-sheet mems deformable mirror for high-contrast imaging," *Journal of Micro/Nanolithography, MEMS, and MOEMS*, vol. 8, no. 3, p. 031308, 2009.

[15] T. G. Bifano, J. A. Perreault, and P. A. Bierden, "Micromachined deformable mirror for optical wavefront compensation," in *International Society for Optics and Photonics, High-Resolution Wavefront Control: Methods, Devices, and Applications II*, vol. 4124, pp. 7–15, 2000.

[16] E. J. Fernández and P. Artal, "Membrane deformable mirror for adaptive optics: performance limits in visual optics," *Optics express*, vol. 11, no. 9, pp. 1056–1069, 2003.

[17] E. Dalimier and C. Dainty, "Comparative analysis of deformable mirrors for ocular adaptive optics," *Optics express*, vol. 13, no. 11, pp. 4275–4285, 2005.

[18] H. Pagès, T. Antonini, T. Aribi, M. Aubry, A. Bastard, E. Beaufort, R. Cousty, G. Dutey, C. Grèzes-Besset, D. Groëninck, *et al.*, "Developments of piezo deformable mirrors," in *Adaptive Optics Systems V*, vol. 9909, p. 99097Z, International Society for Optics and Photonics, 2016.

[19] "Deformable mirrors and adaptive optics." https://www.cilas.com/en/adaptive-mirrors. Accessed: 2018-07-10.

[20] K. Banerjee, P. Rajaeipour, Ç. Ataman, and H. Zappe, "Piezoelectric pvdf actuated, lightweight deformable thin mirror for adaptive optics," in *International Conference on Optical MEMS and Nanophotonics (OMN)*, pp. 1–2, IEEE, 2016.

[21] D. A. Horsley, H. Park, S. P. Laut, and J. S. Werner, "Characterization for vision science applications of a bimorph deformable mirror using phase-shifting interferometry," 2005.

[22] B. R. Oppenheimer, D. L. Palmer, R. G. Dekany, A. Sivaramakrishnan, M. A. Ealey, and T. R. Price, "Investigating a xinξtics inc. deformable mirror," in *International Society for Optics and Photonics, Adaptive Optics and Applications*, vol. 3126, pp. 569–580, International Society for Optics and Photonics, 1997.

[23] E. J. Fernández, L. Vabre, B. Hermann, A. Unterhuber, B. Považay, and W. Drexler, "Adaptive optics with a magnetic deformable mirror: applications in the human eye," *Optics Express*, vol. 14, no. 20, pp. 8900–8917, 2006.

[24] R. J. Zawadzki, S. M. Jones, S. Pilli, S. Balderas-Mata, D. Y. Kim, S. S. Olivier, and J. S. Werner, "Integrated adaptive optics optical coherence tomography and adaptive optics scanning laser ophthalmoscope system for simultaneous cellular resolution in vivo retinal imaging," *Biomedical optics express*, vol. 2, no. 6, pp. 1674–1686, 2011.

[25] H. Hofer, L. Chen, G.-Y. Yoon, B. Singer, Y. Yamauchi, and D. R. Williams, "Improvement in retinal image quality with dynamic correction of the eyes aberrations," *Optics express*, vol. 8, no. 11, pp. 631–643, 2001.

[26] J. W. Evans, K. Morzinski, S. Severson, L. Poyneer, B. Macintosh, D. Dillon, L. Reza, D. Gavel, D. Palmer, S. Olivier, *et al.*, "Extreme adaptive optics testbed: performance and characterization of a 1024-mems deformable mirror," in *International Society for Optics and Photonics, MEMS/MOEMS Components and their applications III*, vol. 6113, p. 61130I, 2006.

[27] J. B. Stewart, A. Diouf, Y. Zhou, and T. G. Bifano, "Open-loop control of a mems deformable mirror for large-amplitude wavefront control," *JOSA A*, vol. 24, no. 12, pp. 3827–3833, 2007.

[28] A. Diouf, A. P. Legendre, J. B. Stewart, T. G. Bifano, and Y. Lu, "Open-loop shape control for continuous microelectromechanical system deformable mirror," *Applied Optics*, vol. 49, no. 31, pp. G148–G154, 2010.

[29] C. Blain, R. Conan, C. Bradley, and O. Guyon, "Open-loop control demonstration of micro-electro-mechanical-system mems deformable mirror," *Optics express*, vol. 18, no. 6, pp. 5433–5448, 2010.

[30] Y. Zhou and T. Bifano, "Characterization of contour shapes achievable with a mems deformable mirror," in *International Society for Optics and Photonics, MEMS/MOEMS Components and Their Applications III*, vol. 6113, p. 61130H, 2006.

[31] N. Devaney, D. Coburn, C. Coleman, J. C. Dainty, E. Dalimier, T. Farrell, D. Lara, D. Mackey, and R. Mackey, "Characterisation of mems mirrors for use in atmospheric and ocular wavefront correction," in *International Society for Optics and Photonics, MEMS Adaptive Optics II*, vol. 6888, p. 688802, International Society for Optics and Photonics, 2008.

[32] N. Devaney, E. Dalimier, T. Farrell, D. Coburn, R. Mackey, D. Mackey, F. Laurent, E. Daly, and C. Dainty, "Correction of ocular and atmospheric wavefronts: a comparison of the performance of various deformable mirrors," *Applied optics*, vol. 47, no. 35, pp. 6550–6562, 2008.

[33] S. Cornelissen, P. Bierden, and T. Bifano, "Development of a 4096 element mems continuous membrane deformable mirror for high contrast astronomical imaging," in *International Society for Optics and Photonics, Advanced Wavefront Control: Methods, Devices, and Applications IV*, vol. 6306, p. 630606, 2006.

[34] G. Vdovin and P. Sarro, "Flexible mirror micromachined in silicon," *Applied optics*, vol. 34, no. 16, pp. 2968–2972, 1995.

[35] D.-Y. Qiao, S.-J. Wang, and W.-Z. Yuan, "A continuous-membrane micro deformable mirror based on anodic bonding of soi to glass wafer," *Microsystem technologies*, vol. 16, no. 10, pp. 1765–1769, 2010.

[36] M. J. Moghimi, B. J. Lutzenberger, B. M. Kaylor, and D. L. Dickensheets, "Moems deformable mirrors for focus control in vital microscopy," *Journal of Micro/Nanolithography, MEMS, and MOEMS*, vol. 10, no. 2, p. 023005, 2011.

[37] M. Strathman, Y. Liu, E. G. Keeler, M. Song, U. Baran, J. Xi, M.-T. Sun, R. Wang, X. Li, and L. Y. Lin, "Mems scanning micromirror for optical coherence tomography," *Biomedical optics express*, vol. 6, no. 1, pp. 211–224, 2015.

[38] N. Doble, D. T. Miller, G. Yoon, and D. R. Williams, "Requirements for discrete actuator and segmented wavefront correctors for aberration compensation in two large populations of human eyes," *Applied optics*, vol. 46, no. 20, pp. 4501–4514, 2007.

[39] Z. Liu, O. P. Kocaoglu, and D. T. Miller, "In-the-plane design of an off-axis ophthalmic adaptive optics system using toroidal mirrors," *Biomedical optics express*, vol. 4, no. 12, pp. 3007–3030, 2013.

[40] R. S. Jonnal, O. P. Kocaoglu, R. J. Zawadzki, Z. Liu, D. T. Miller, and J. S. Werner, "A review of adaptive optics optical coherence tomography: technical advances, scientific applications, and the future," *Investigative ophthalmology & visual science*, vol. 57, no. 9, pp. OCT51–OCT68, 2016.

[41] J. Liang, D. R. Williams, and D. T. Miller, "Supernormal vision and high-resolution retinal imaging through adaptive optics," *JOSA A*, vol. 14, no. 11, pp. 2884–2892, 1997.

[42] D. T. Miller, L. N. Thibos, and X. Hong, "Requirements for segmented correctors for diffraction-limited performance in the human eye," *Optics express*, vol. 13, no. 1, pp. 275–289, 2005.

[43] Y. Zhang, J. Rha, R. S. Jonnal, and D. T. Miller, "Adaptive optics parallel spectral domain optical coherence tomography for imaging the living retina," *Optics Express*, vol. 13, no. 12, pp. 4792–4811, 2005.

[44] Y. Zhang, B. Cense, J. Rha, R. S. Jonnal, W. Gao, R. J. Zawadzki, J. S. Werner, S. Jones, S. Olivier, and D. T. Miller, "High-speed volumetric imaging of cone photoreceptors with adaptive optics spectral-domain optical coherence tomography," *Optics Express*, vol. 14, no. 10, pp. 4380–4394, 2006.

[45] J. Rha, R. S. Jonnal, K. E. Thorn, J. Qu, Y. Zhang, and D. T. Miller, "Adaptive optics flood-illumination camera for high speed retinal imaging," *Optics express*, vol. 14, no. 10, pp. 4552–4569, 2006.

[46] Q. Wang, O. P. Kocaoglu, B. Cense, J. Bruestle, R. S. Jonnal, W. Gao, and D. T. Miller, "Imaging retinal capillaries using ultrahigh-resolution optical coherence tomography and adaptive optics," *Investigative ophthalmology & visual science*, vol. 52, no. 9, pp. 6292–6299, 2011.

[47] R. J. Zawadzki, Y. Zhang, S. M. Jones, R. D. Ferguson, S. S. Choi, B. Cense, J. W. Evans, D. Chen, D. T. Miller, S. S. Olivier, *et al.*, "Ultrahigh-resolution adaptive optics-optical coherence tomography: toward isotropic 3 μm resolution for in vivo retinal imaging," in *Coherence Domain Optical Methods and Optical Coherence Tomography in Biomedicine XI*, vol. 6429, p. 642909, International Society for Optics and Photonics, 2007.

[48] R. J. Zawadzki, Y. Zhang, S. M. Jones, S. S. Choi, B. Cense, D. Chen, A. R. Fuller, D. T. Miller, S. S. Olivier, and J. S. Werner, "Application of adaptive optics: optical coherence tomography for in vivo imaging of microscopic structures in the retina and optic nerve head," in *Ophthalmic Technologies XVII*, vol. 6426, p. 64261O, International Society for Optics and Photonics, 2007.

[49] Y. Jian, R. J. Zawadzki, and M. V. Sarunic, "Adaptive optics optical coherence tomography for in vivo mouse retinal imaging," *Journal of biomedical optics*, vol. 18, no. 5, p. 056007, 2013.

[50] Y. Jian, A. Issaei, R. J. Zawadzki, and M. V. Sarunic, "Adaptive optics: optical coherence tomography system for in-vivo imaging of the mouse retina," in *Optical Coherence Tomography and Coherence Domain Optical Methods in Biomedicine XVI*, vol. 8213, p. 82130L, International Society for Optics and Photonics, 2012.

[51] A. Zam, P. Zhang, Y. Jian, M. V. Sarunic, S. Bonora, E. N. Pugh, and R. J. Zawadzki, "Progress on developing wavefront sensorless adaptive optics optical coherence tomography for in vivo retinal imaging in mice," in *Optical Coherence Tomography and Coherence Domain Optical Methods in Biomedicine XIX*, vol. 9312, p. 93122I, International Society for Optics and Photonics, 2015.

[52] D. J. Wahl, S. Bonora, O. S. Mata, B. K. Haunerland, R. J. Zawadzki, M. V. Sarunic, and Y. Jian, "Wavefront sensorless approaches to adaptive optics for in vivo fluorescence imaging of mouse retina," in *Adaptive Optics and Wavefront Control for Biological Systems II*, vol. 9717, p. 97170A, International Society for Optics and Photonics, 2016.

[53] M. J. Ju, M. Heisler, D. Wahl, Y. Jian, and M. V. Sarunic, "Multiscale sensorless adaptive optics oct angiography system for in vivo human retinal imaging," *Journal of biomedical optics*, vol. 22, no. 12, p. 121703, 2017.

[54] L. Rizzotto, S. Bonora, Y. Jian, P. Zhang, A. Zam, E. N. Pugh, F. Mammano, R. J. Zawadzki, and M. V. Sarunic, "Comparison of a novel adaptive lens with deformable mirrors and its application in high-resolution in-vivo oct imaging," in *Adaptive Optics and Wavefront Control for Biological Systems*, vol. 9335, p. 933514, International Society for Optics and Photonics, 2015.

[55] Y. Jian, J. Xu, M. A. Gradowski, S. Bonora, R. J. Zawadzki, and M. V. Sarunic, "Wavefront sensorless adaptive optics optical coherence tomography for in vivo retinal imaging in mice," *Biomedical optics express*, vol. 5, no. 2, pp. 547–559, 2014.

[56] K. S. Wong, Y. Jian, M. Cua, S. Bonora, R. J. Zawadzki, and M. V. Sarunic, "In vivo imaging of human photoreceptor mosaic with wavefront sensorless adaptive optics optical coherence tomography," *Biomedical optics express*, vol. 6, no. 2, pp. 580–590, 2015.

[57] R. J. Zawadzki, S. S. Choi, S. M. Jones, S. S. Oliver, and J. S. Werner, "Adaptive optics-optical coherence tomography: optimizing visualization of microscopic retinal structures in three dimensions," *JOSA A*, vol. 24, no. 5, pp. 1373–1383, 2007.

[58] D. J. Wahl, C. Huang, S. Bonora, Y. Jian, and M. V. Sarunic, "Pupil segmentation adaptive optics for invivo mouse retinal fluorescence imaging," *Optics letters*, vol. 42, no. 7, pp. 1365–1368, 2017.

[59] R. J. Zawadzki, S. M. Jones, S. S. Olivier, M. Zhao, B. A. Bower, J. A. Izatt, S. Choi, S. Laut, and J. S. Werner, "Adaptive-optics optical coherence tomography for high-resolution and high-speed 3d retinal in vivo imaging," *Optics express*, vol. 13, no. 21, pp. 8532–8546, 2005.

[60] R. J. Zawadzki, S. M. Jones, S. Pilli, D. Y. Kim, S. S. Olivier, and J. S. Werner, "Retinal imaging with a combined adaptive optics/optical coherence tomography and adaptive optics/scanning laser ophthalmoscopy system," in *Ophthalmic Technologies XX*, vol. 7550, p. 75500Z, International Society for Optics and Photonics, 2010.

[61] R. J. Zawadzki, P. Zhang, A. Zam, E. B. Miller, M. Goswami, X. Wang, R. S. Jonnal, S.-H. Lee, D. Y. Kim, J. G. Flannery, *et al.*, "Adaptive-optics slo imaging combined with widefield oct and slo enables precise 3d localization of fluorescent cells in the mouse retina," *Biomedical optics express*, vol. 6, no. 6, pp. 2191–2210, 2015.

[62] A. Panorgias, R. J. Zawadzki, A. G. Capps, A. A. Hunter, L. S. Morse, and J. S. Werner, "Multimodal assessment of microscopic morphology and retinal function in patients with geographic atrophy," *Investigative ophthalmology & visual science*, vol. 54, no. 6, pp. 4372–4384, 2013.

[63] O. P. Kocaoglu, T. L. Turner, Z. Liu, and D. T. Miller, "Adaptive optics optical coherence tomography at 1 mhz," *Biomedical optics express*, vol. 5, no. 12, pp. 4186–4200, 2014.

[64] R. J. Zawadzki, B. Cense, Y. Zhang, S. S. Choi, D. T. Miller, and J. S. Werner, "Ultrahigh-resolution optical coherence tomography with monochromatic and chromatic aberration correction," *Optics Express*, vol. 16, no. 11, pp. 8126–8143, 2008.

[65] J. W. Evans, R. J. Zawadzki, S. M. Jones, S. S. Olivier, and J. S. Werner, "Error budget analysis for an adaptive optics optical coherence tomography system," *Optics express*, vol. 17, no. 16, pp. 13768–13784, 2009.

[66] T. G. Bifano, J. Perreault, R. K. Mali, and M. N. Horenstein, "Microelectromechanical deformable mirrors," *IEEE Journal of Selected Topics in Quantum Electronics*, vol. 5, no. 1, pp. 83–89, 1999.

[67] C. Blain, R. Conan, C. Bradley, O. Guyon, and C. Vogel, "Characterisation of the influence function non-additivities for a 1024-actuator mems deformable mirror," in *EDP Sciences, 1st AO4ELT conference-Adaptive Optics for Extremely Large Telescopes*, p. 06009, 2010.

[68] C. C. Zhang, W. B. Foster, R. D. Downey, C. L. Arrasmith, and D. L. Dickensheets, "Dynamic performance of mems deformable mirrors for use in an active/adaptive two-photon microscope," in *International Society for Optics and Photonics, Adaptive Optics and Wavefront Control for Biological Systems II*, vol. 9717, p. 97170G, 2016.

[69] J. Porter, A. Guirao, I. G. Cox, and D. R. Williams, "Monochromatic aberrations of the human eye in a large population," *JOSA A*, vol. 18, no. 8, pp. 1793–1803, 2001.

[70] Micralyne, Inc., "Micragem-si platform design handbook (ver.1.3)," April 20, 2016.

[71] B.-G. Jeong, D.-K. Kim, S.-W. Hong, S.-W. Chung, and H.-J. Shin, "Performance and reliability of new cmut design with improved efficiency," *Sensors and Actuators A: Physical*, vol. 199, pp. 325–333, 2013.

[72] R. Zengerle, A. Richter, and H. Sandmaier, "A micro membrane pump with electrostatic actuation," in *[1992] Proceedings IEEE Micro Electro Mechanical Systems*, pp. 19–24, IEEE, 1992.

[73] P.-C. Hsu, C. Mastrangelo, and K. Wise, "A high sensitivity polysilicon diaphragm condenser microphone," in *Proceedings MEMS 98. IEEE. Eleventh Annual International Workshop on Micro Electro Mechanical Systems. An Investigation of Micro Structures, Sensors, Actuators, Machines and Systems (Cat. No. 98CH36176*, pp. 580–585, IEEE, 1998.

[74] X. Zhang, F. Chau, C. Quan, Y. Lam, and A. Liu, "A study of the static characteristics of a torsional micromirror," *Sensors and Actuators A: Physical*, vol. 90, no. 1-2, pp. 73–81, 2001.

APPENDICES

Appendix A

Copyrights

March 18, 2020

Name of Publication: Dynamic Adaptive Mirror **(**the "Work")

Author: Amr Kamel

Publisher: University of Waterloo, Ontario, Canada - "Thesis" **(**the "Publisher")

Description or sample of Material: Diagrams from MEMS-Based Deformable Mirrors Page (Types of Aberrations Tab on 3258) (the "Material")

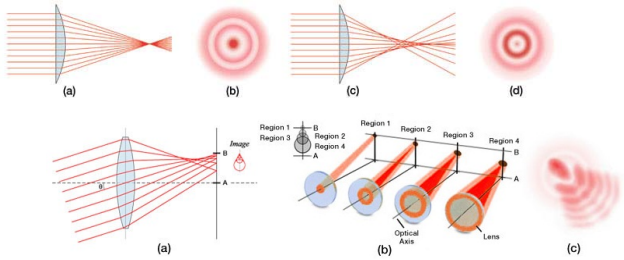

Thorlabs, Inc. hereby grants permission to Publisher under a Creative Commons Attribution License (CC BY) to include the Material in the Work, and in all future editions and revisions thereof, without restriction, and to create derivative and ancillary works therefrom for research and academic purposes only subject to making such derivative work generally available under the grant of a similar license , and to publish such derivative work in all media now known or hereafter discovered throughout the world and in all languages, whether published by the university of Waterloo (the "Publisher") or its licensees.

A credit line to acknowledge use of the material is required and shall reference "Thorlabs, Inc." and the product part number(s).

Agreed and Accepted:
THORLABS, INC.

By: Robert P. Regimbal

Date: 3/19/20

Name: Robert P. Regimbal

Title: CFO

Figure A.1: THORLABS Consent

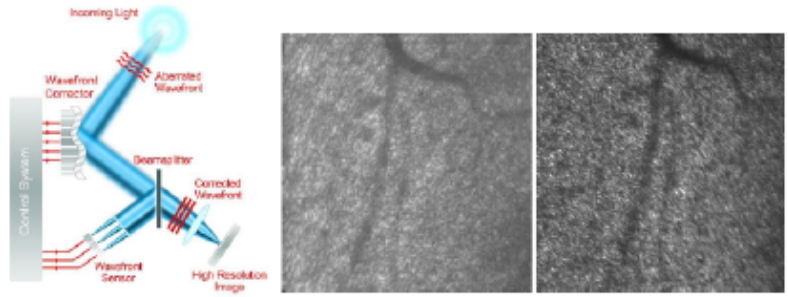

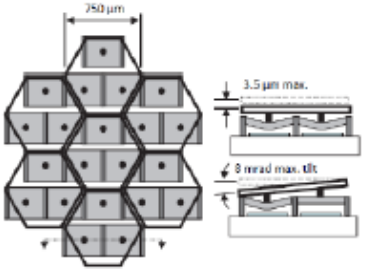

I will send you a copy after my defense date April 29, 2020.

Best Regards,

Amr,

From: Philip Zeng <pzeng@bostonmicromachines.com>
Sent: 05 March 2020 13:56
To: Amr Kamel
Cc: Michael R. Feinberg; Kevin Flavin
Subject: RE: Permission_Copyright

Dear Amr,

Thank you for reaching out to Boston Micromachines.

Figure A.2: BostonMicromachines Consent

RE: University of Waterloo Student IP request

Zoetewey, David J <David.Zoetewey@Teledyne.com>

Fri 08/05/2020 15:20

To: Amr Kamel <amr.kamel@uwaterloo.ca>;

Cc: Hunsaker, Zachary <Zachary.Hunsaker@Teledyne.com>; Williams, Miles R (INT) <Miles.Williams@Teledyne.com>;

Amr,

You have Teledyne Micralyne Inc.'s permission to use and modify Figure 7 on page 12, copied below, of the Teledyne Micralyne Design Handbook titled "MicraGEM-Si Platform" (the "Figure") in your thesis on the topic of "Resonant adaptive mirrors" for the University of Waterloo, and Teledyne also grants the University of Waterloo permission to publish the Figure as part of that thesis, provided however, that your use of the Figure is not used in a manner that conveys false or inaccurate information and does not negatively impact the reputation of Teledyne Micralyne or its affiliates, customers, or vendors or their respective products.

Best regards,

David

David Zoetewey
Chief Intellectual Property Counsel
Teledyne Technologies Incorporated
1049 Camino Dos Rios, CA 91360
David.Zoetewey@Teledyne.com
+1-805-373-4244

From: Amr Kamel <amr.kamel@uwaterloo.ca>
Sent: Friday, May 8, 2020 10:32 AM
To: Zoetewey, David J <David.Zoetewey@Teledyne.com>
Cc: Hunsaker, Zachary <Zachary.Hunsaker@Teledyne.com>; Williams, Miles R (INT) <Miles.Williams@Teledyne.com>
Subject: Re: University of Waterloo Student IP request

External Email

Hello David,

No, it is not.
I have used the design handbook page 12. Please, see the attached file. Also, I have added an annotations to the figure for clarifications. I include the design handbook to my references into the thesis.

Figure A.3: MicraGEM Consent